Journal of Computational Applied Mechanics 2026, 57(2): 230-256

DOI: 10.22059/jcamech.2025.406447.1694

RESEARCH PAPER

CFD simulation of turbulent aerodynamics of a hummingbird wing for gliding micro-UAVs

Muhammad Junaid Akbar [a], Osman Anwar Bég [b], Tasveer Anwar Bég [c], Muhammad Mubashir Bhatti [d,e,*], Ali Kadir [b], Sireetorn Kuharat [b]

[a] *Aeronautical and Mechanical Engineering Department, SEE Building, University of Salford, Manchester, M54WT, UK*
[b] *Multi-Physical Engineering Sciences Group, Mechanical Engineering Department, Corrosion and Coatings Lab, Room 3-08, SEE Building, University of Salford, Manchester, M54WT, UK*
[c] *Engineering Mechanics Research, Israfil House, Dickenson Rd., Manchester, M13, UK*
[d] *Department of Physics, College of Science, Korea University, 145 Anam-ro, Seongbuk-gu, Seoul 02841, Republic of Korea*
[e] *Material Science Innovation and Modelling (MaSIM) Research Focus Area, North-West University (Mafikeng Campus), Private Bag X2046, Mmabatho 2735, South Africa*

Abstract

Bio-inspired wing geometries provide a promising pathway for enhancing the aerodynamic efficiency of micro–air vehicles (MAVs), particularly in low-Reynolds-number flight regimes. This study presents a detailed computational analysis of turbulent airflow over a hummingbird-inspired wing operating in gliding conditions, focusing on the aerodynamic mechanisms essential for micro-UAV design. A simplified, biologically motivated wing planform—preserving the characteristic aspect ratio and chord distribution while omitting feather-level complexity—is modelled to isolate the dominant flow physics. Numerical simulations are performed using ANSYS FLUENT with the k–ε turbulence model to evaluate lift, drag, pressure distribution, and flow topology across inlet velocities of 5, 10, and 15 m/s. The results show that the hummingbird-based wing maintains stable aerodynamic performance under all flow conditions, with lift increasing steadily with velocity and peaking at 15 m/s, accompanied by the expected drag augmentation. Pressure and velocity fields confirm the formation of biologically consistent high-pressure regions beneath the wing and low-pressure zones above it, intensifying with increasing speed. A comparative assessment of full-wing and symmetry-based half-wing simulations demonstrates that the latter accurately reproduces aerodynamic trends while substantially reducing computational cost. The findings offer actionable insights into the development of efficient gliding micro-UAVs inspired by natural flyers and establish a foundation for future research in flapping-wing aerodynamics and aeroelastic fluid–structure interaction (FSI).

Keywords: Bio-inspired aerodynamics; Bio-inspired aerodynamics; Micro air vehicles (MAVs); Gliding flight; Low-Reynolds-number aerodynamics; Computational fluid dynamics (CFD)

* Corresponding author.
E-mail address: mmbhatti@korea.ac.kr

1. Graphical Abstract

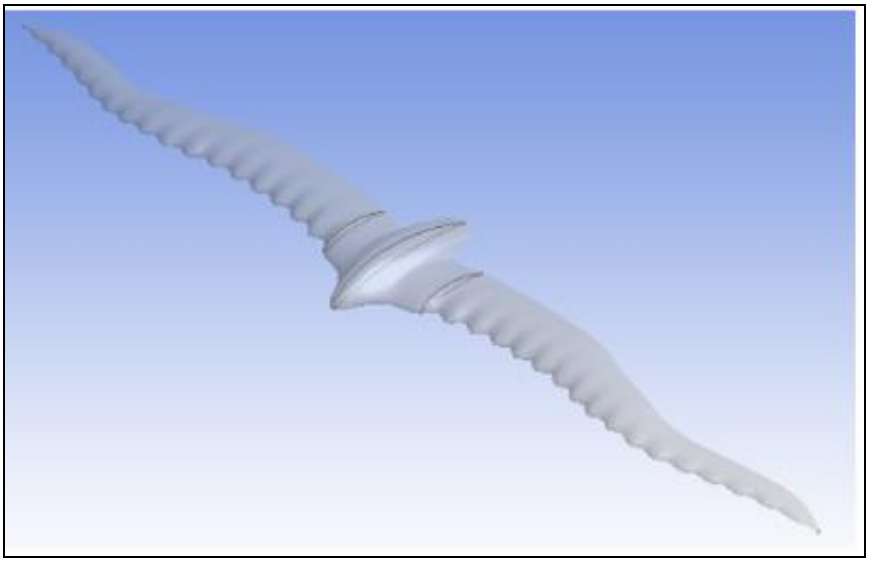

2. Nomenclature

List of Abbreviations	
Re	Reynolds Number
AoA	Angle of Attack
UAV	Unmanned Aerial Vehicle
MAV	Micro Aerial Vehicle
FWMAV	Flapping Wing Micro Aerial Vehicle
CFD	Computational Fluid Dynamics
FSI	Fluid Structure Interaction
List of Symbols	
α	Angle of Attack (Degrees)
V	Inlet Velocity (*m/s*)
L	Lift Force (Newtons)
D	Drag Force (Newtons)
C_L	Lift Coefficient
C_D	Drag Coefficient
$L-D$	Lift to Drag Ratio
P	Pressure (Pascals)
μ	Dynamic Viscosity (Pa.s)
ρ	Density of Air (kg/m^3)
ω	Specific dissipation rate (s^{-1})
A	Wing Area
ν	Kinematic Viscosity $\left(m^2/s\right)$
C	Chord Length (m)
ε	Turbulence dissipation rate (m^2/s^3)

3. Introduction

The remarkable flight capabilities of birds and insects have long inspired researchers seeking to replicate nature's aerodynamic efficiency in engineered systems [1]. This area has come to be known as bio-inspired aerodynamics [2]. next generation elegant mechanisms observed in nature, the flapping-wing mechanism of birds offers exceptional manoeuvrability, stability and lift generation under low Reynolds number conditions, making it an ideal model for next-generation unmanned aerial vehicles (UAVs). Unlike traditional fixed-wing or rotary-wing aircraft, flapping-wing UAVs, often termed micro aerial vehicles (MAVs), are capable of precise control in confined or turbulent environments, owing to their ability to hover, perform agile turns, and operate at low speeds with minimal noise [3].

The pursuit of bio-inspired flight has gained momentum with advancements in materials, sensors, and computational modelling. By mimicking the wing kinematics of natural flyers, researchers have attempted to bridge the gap between biological elegance and mechanical performance [4-6]. Many different bird species have been studied including owls (for sound suppression) [7], gliding of white storks [8], pigeon wings [9, 10]. These have generated various developments including bionic slats for owl-inspired wings [11] and serrated wing designs aimed at reducing aero-acoustic effects [12]. Withers [13] has shown that bird wings demonstrate a trade-off between lift and drag performance; wings with low drag exhibit low maximum lift coefficients whereas wings possessing high drag are associated with much higher maximum lift coefficients. He has also highlighted that aerodynamics of bord wings as characterized by pressure-distribution data, concur with aerodynamic theory for UAV and aircraft wings at low Reynolds numbers, and produce similar lift and drag coefficients for comparable geometric scales. In the case of micro- UAVs, particular attention has been paid to small flyers such as hummingbirds and house flies, whose wing motions present a rich foundation for aerodynamics research. Hummingbird aerodynamics has been investigated by Altshuler and Dudley [14] and Nakata *et al.* [15]. These studies have shown that hummingbirds can sustain efficient hovering, enabled by high-frequency wingbeats and unique stroke patterns that generate lift on both downstroke and upstroke. Their ability to control flight direction mid-air, as well as their stability during hover, makes them an ideal biological model for UAV design. Hummingbirds possess a unique musculoskeletal structure that allows them to flap their wings in a near-horizontal plane, enabling sustained hovering and backward flight. Unlike most birds, both the downstroke and upstroke generate lift due to their symmetric figure-eight wingbeat pattern. The wings beat at a moderate frequency of 40–60 Hz with a stroke amplitude of approximately 120 degrees. Conversely, house flies demonstrate an entirely different class of unsteady aerodynamics [16]. Operating at much lower Reynolds numbers, they rely on mechanisms such as clap-and-fling and rapid pronation/supination of the wings to generate high lift forces. The flexible structure of their wings, combined with fast stroke cycles, allows them to respond quickly to disturbances, making them highly efficient in evasive and agile flight. Lift production in hummingbirds during the upstroke is nearly as significant as during the downstroke, owing to wing rotation and spanwise twist, resulting in a quasi-steady aerodynamic effect. These mechanisms, while biologically optimised, are difficult to replicate mechanically and pose significant challenges in modelling and control. Despite progress in physical prototyping, the aerodynamic analysis of flapping-wing UAVs remains complex due to the unsteady, three-dimensional nature of the flow. Traditional theories fall short in predicting the dynamic interactions between wing motion and air, particularly at the scales and frequencies relevant to MAVs. In this context, Computational Fluid Dynamics (CFD) has emerged as a vital simulation tool for analysing both gliding and flapping-wing aerodynamics. It allows researchers to simulate intricate flow structures, such as leading-edge vortices and wake capture, providing deeper insight into lift generation, energy efficiency, and overall performance. Recent years have witnessed a transformative shift towards highly detailed, multidisciplinary CFD simulations incorporating both biological realism and engineering innovation. With increasing computational power, researchers have successfully modelled full-cycle flapping dynamics of hummingbirds and houseflies, accounting for flexible wing deformation, FSI, and vortex shedding patterns. These aspects have been addressed by Nakata *et al.* [15] and Zhu and Zhang [17]. Hummingbirds can maintain stable hover in turbulent conditions, making them ideal models for autonomous UAVs operating in confined spaces. CFD simulations have demonstrated that unsteady forces, such as clap-and-fling and added mass effects, play significant roles in lift augmentation during hummingbird hovering, as noted by Song *et al.* [18]. Similarly, houseflies have inspired designs involving rapid frequency modulation and asymmetrical stroke patterns for precise flight control, as examined by Liu and Sun [19].

Although substantial work has been done to characterize aerodynamic forces in bio-inspired flapping systems, significant research gaps persist in understanding the coupling between wing flexibility, energy efficiency, and stability in varying environmental conditions. Also *gliding aerodynamics* has not received extensive attention and remains a key aspect in fixed wing micro-UAV designs, and this is a major novelty of the present study. The Reynolds number for hummingbird flight ranges between 1,000 and 5,000, placing it in a transitional regime where both laminar and turbulent flow features may coexist. As such, CFD studies often employ transitional turbulence models or large eddy simulation (LES) to resolve the unsteady vortical structures. Recent CFD analyses, such as those conducted by Dong *et al.* [20], reported on CFD ANSYS FLUENT modelling of a three-dimensional wing model with dynamic morphing, showing the high contribution of rotational lift near stroke reversal.

While many studies have examined the hovering and flapping aerodynamics of hummingbirds [18], relatively few investigations have considered gliding flight. In many UAV designs gliding is critical as the wings are fixed and do not flap. This is the motivation for the present study. Hummingbirds do not glide in the same way other birds do; instead, they achieve flight through a unique wing rotation that resembles a figure-eight motion. This allows them to generate lift on both the upstroke and downstroke, enabling them to hover, fly backward, and move in any direction.

They achieve this highly agile flight by rapidly rotating their wings and shoulders. However, the potential benefits of using hummingbird inspired wings for gliding have not yet been reported. We deploy ANSYS FLUENT software [21]. Turbulent flow is considered and the k-epsilon model deployed. Velocity and pressure contours are visualized for a range of gliding velocities. A key focus is how variations in angle of attack and airflow velocity influence aerodynamic performance. Lift and drag behaviour are also studied. The simulations provide a foundation for future CFD simulations featuring flapping and aeroelastic behaviour (with flexible wings) of direct relevance to hummingbird inspired micro-UAV designs [22, 23].

4. Flow model and computational methodology

CFD studies relevant to biologically inspired flyers have examined various parameters, from wing kinematics and stroke amplitude to material flexibility and deformation. These simulations provide insight into how small-scale flyers, such as hummingbirds, operate efficiently at low to moderate Reynolds numbers. By capturing pressure distributions, streamline patterns, vorticity fields and force histories, CFD allows the optimisation of wing design for improved performance, manoeuvrability, and energy efficiency in UAV applications. In this article, ANSYS FLUENT has been deployed to solve the turbulent flow with the k-epsilon model for a 3-D gliding hummingbird wing inspired planform. Details of the formulations are omitted here for brevity. The wing geometry for this study was inspired by the hummingbird, chosen due to its exceptional hovering capabilities, high manoeuvrability, and extensive aerodynamic research available in existing literature. These characteristics make it an ideal biological model for informing the design of bio-inspired flapping wing micro aerial vehicles (FWMAVs). The hummingbird's unique ability to sustain lift during both the downstroke and upstroke phases offers a rich aerodynamic foundation for CFD analysis. For the purposes of this study, the wing was modelled in 3D to represent the general planform, aspect ratio, and chord distribution of a hummingbird wing, while simplifying complex morphological details such as individual feather structure. This simplification ensured that the computational model remained focused on capturing key aerodynamic mechanisms—such as leading-edge vortex (LEV) stability, wake capture, and rotational circulation—without introducing unnecessary geometric complexity that would increase computational cost. In hummingbirds, the wing's structural flexibility, combined with rapid wingbeat frequencies, plays a major role in aerodynamic efficiency. However, modelling fully flexible, feathered wings with precise material properties requires high-resolution fluid–structure interaction (FSI) simulations, which can be computationally expensive and are beyond the scope of the current study, although they are being considered for future investigations. Given the limitations of available computational resources, this study adopted a rigid wing assumption while preserving the overall kinematic motion derived from literature-based measurements of hummingbird wingbeats.

4.1. Geometry Selection & Simplification

Table 1 Below shows the geometric properties of the hummingbird wing retrieved from [24].

Table 1: Hummingbird Area Properties

	Aspect Ratio (AR)	Area, S (mm^2)	Centroid X (mm)	Centroid Y	Length R (mm)	Chord C (mm)
AVG	11.43	984.3	22.45	15.54	72.45	29.86
STD	0.22	104.6	6.43	4.35	7.56	6.31
MAX	19.65	1100.54	34.86	34.64	62.34	38.45
MIN	17.42	742	12.22	9.22	54.32	32.22

Error! Reference source not found.**2** Below shows the air properties and conditions implemented in this study.

Table 2: Conditions and properties employed for simulations

Conditions	Properties
Atmospheric Fluid	Air
Atmospheric Temperature	288 K
Density of Air	1.255 kg/m^3
Simulated Velocities	5, 10, 15 *m/s*

No slip velocity conditions, standard atmospheric pressure (1 atmosphere i.e. 10^5Pa) are imposed at the wing surface and inlet velocity is varied as per **Table 2** above.

4.2. Overview of ANSYS Fluent Process, Flow Equations and Turbulence Settings

This section details the step-by-step procedure followed for simulating airflow around the hummingbird-inspired wing using ANSYS Fluent. The assumptions are incompressible, turbulent, low Mach number aerodynamic flow, with constant atmospheric pressure and no slip at the wing surface. The governing equations, i.e. Navier-Stokes equations take the form [26] of the continuity and momentum conservation equations. The conservation of mass is

given as Eqn. 1. Eqn. 2 gives the conservation of momentum, $\partial v/\partial t$ is representative of the speed variation over time (of the fluid), the $v\nabla v$ term is indicative of both fluid speed and direction, ∇P is the pressure change within the fluid, ρg is the buoyancy force representing the external forces acting on the fluid, and finally. The diffusion term $\nabla^2 v$ is defined by the viscous stresses acting on the fluid:

$$\frac{\partial \rho}{\partial t} + \nabla \rho v = 0, \tag{1}$$

$$\rho\left(\frac{\partial v}{\partial t} + v\nabla v\right) = -\nabla p + \rho g + \mu \nabla^2 v, \tag{2}$$

Here ρ is the fluid density (kg/m^3), u is the velocity field vector (m/s), t is the time (s), p is the pressure field (N/m^2), g is gravitational acceleration (m/s^2), μ is the dynamic viscosity of the fluid ($kg/m\ s$). We use the pressure-based solver (incompressible flow) and utilize the SIMPLE algorithm which iteratively solves Navier-Stokes equations for incompressible flows by treating pressure gradient terms implicitly. ANSYS Fluent uses it for steady-state fluid flow simulations, sequentially updating pressure and velocity to ensure convergence across various engineering scenarios. The step-by-step procedure involves first setting up boundary conditions, then computing velocity and pressure gradients, computing intermediate velocity field to solve the discretised momentum equation, then calculating uncorrected mass fluxes at faces, next solving the pressure correction equation to produce cell values of the pressure condition, updating the pressure field, update the boundary pressure conditions, correcting the face mass fluxes, cell velocities correction, and finally updating density as pressure changes. Turbulence is simulated with the *k-epsilon turbulence model*. This turbulence model furnishes adequate refinement in the velocity field and simultaneously avoids excessive compilation times required with alternate turbulence models (e.g. RNG). The standard *k-epsilon* turbulence is the most common Reynolds Averaged Navier Stokes (**RANS**), two-equation, semi-empirical model which is based on the transport equations for turbulent kinetic energy, k and its dissipation rate ε

$$\frac{\partial}{\partial t}(k\rho) + \frac{\partial}{\partial x_i}(k\rho u_i) = \frac{\partial}{\partial x_j}\left[\left(\mu + \frac{\mu_t}{\sigma_k}\right)\frac{\partial k}{\partial x_j}\right] + G_k + G_b - \rho\varepsilon - Y_M + S_k, \tag{3}$$

$$\frac{\partial}{\partial t}(\varepsilon\rho) + \frac{\partial}{\partial x_i}(\varepsilon\rho u_i) = \frac{\partial}{\partial x_j}\left[\left(\mu + \frac{\mu_t}{\sigma_\varepsilon}\right)\frac{\partial \varepsilon}{\partial x_j}\right] + C_{1\varepsilon}\frac{\varepsilon}{k}\left(G_k + C_{3\varepsilon}G_b\right) - C_{2\varepsilon}\rho\frac{\varepsilon^2}{k} + S_\varepsilon. \tag{4}$$

Physically this model implies the following:

Rate of change of k or ε	+	Transport of k or ε by convection	=	Transport of k or ε by diffusion	+	Rate of production of k or ε	–	Rate of destruction of k or ε

The production and destruction of turbulent kinetic energy are always closely linked- the rate of dissipation is large where the rate of production is large. Here G_k = turbulence kinetic energy generation due to mean velocity gradients, G_b is the generation of turbulence kinetic energy due to buoyancy, Y_M is the contribution of the fluctuating dilatation in compressible turbulence to the overall dissipation rate, $C_{1\varepsilon}, C_{2\varepsilon}, C_{3\varepsilon}$ are constants, σ_k and σ_ε are turbulent Prandtl numbers for k and ε respectively, with values of 1.0 and 1.3 and S_k and S_ε are user-defined source terms. To determine turbulent length and time scale, we deployed test values of 0.05-0.07 times the characteristic length (chord length) for the turbulent length scale and turbulent intensity was tested between 1-10%. *k and* ε were then determined from these more specifically since in ANSYS FLUENT [26], the default *k=1 and* ε*=1*, are often too high. Dissipation rate (ε) was adjusted to match the length scale and prevent premature decay of turbulence. The constants $C_{1\varepsilon}, C_{2\varepsilon}, C_{3\varepsilon}$ were prescribed values of 1.44, 1.92, 0.09, values which are widely accepted for aerodynamics flows [27]. The *k*-epsilon model assumes that the flow is fully turbulent with the effects of molecular viscosity negligible. The *k*-epsilon turbulence model is however only valid for fully turbulent flows and performs poorly when simulating flows with strong separation, high pressure gradients and very large streamline curvature.

The process began by creating the hummingbird-inspired wing geometry directly within ANSYS, avoiding the need for external CAD software. This approach ensured that the geometry could be tailored precisely to the

simulation requirements while streamlining the workflow. Once the geometry was established, a suitable computational mesh was generated to accurately capture the interaction between airflow and the wing surface. Mesh refinement was applied in regions of high aerodynamic importance, such as the leading and trailing edges, to enhance resolution and accuracy. Following mesh generation, the boundary conditions were defined to represent the operational environment of the wing, including inlet velocity profiles and pressure outlet conditions. The k-epsilon model was found to be adequate and appropriate for low Reynolds number flows and reasonably well computes the aerodynamic regime characteristics of hummingbird-inspired micro-UAV wings with reduced compilation times. Of course, more elegant turbulence models are available in ANSYS FLUENT [26] (e.g. k-omega SST, DES etc) but require much higher mesh densities and compilation times and may be explored in the future. Solver parameters were then configured to simulate the airflow over the wing effectively. The stages of the simulations are now described.

4.3. ANSYS FLUENT simulation stages

4.3.1 Geometry Creation

In this study, the wing geometry was obtained as a pre-defined geometry file and directly imported into ANSYS Fluent for processing. This approach eliminated the need for manual sketching and extrusion, allowing the focus to remain on mesh generation, solver settings, and aerodynamic analysis. The geometry was imported in a suitable format and scaled appropriately within ANSYS to ensure accurate representation of the wing dimensions. Once imported, the model was verified for geometric consistency and prepared for the meshing process. Figure 1 below shows the imported geometry of the wing as visualised in ANSYS.

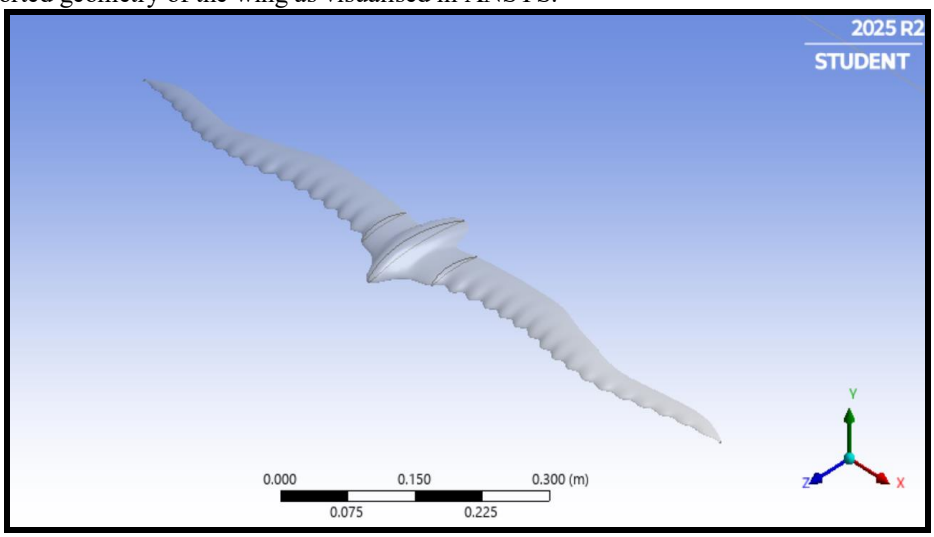

Fig 1: 3D Hummingbird planform geometry Imported into ANSYS

The computational domain dimensions were defined within ANSYS to ensure sufficient space for airflow development around the wing geometry, thereby avoiding any artificial boundary effects. The domain is shown in Fig. 2. Care was taken to balance domain size with the computational limitations of the student edition of ANSYS, which restricts the maximum number of elements.

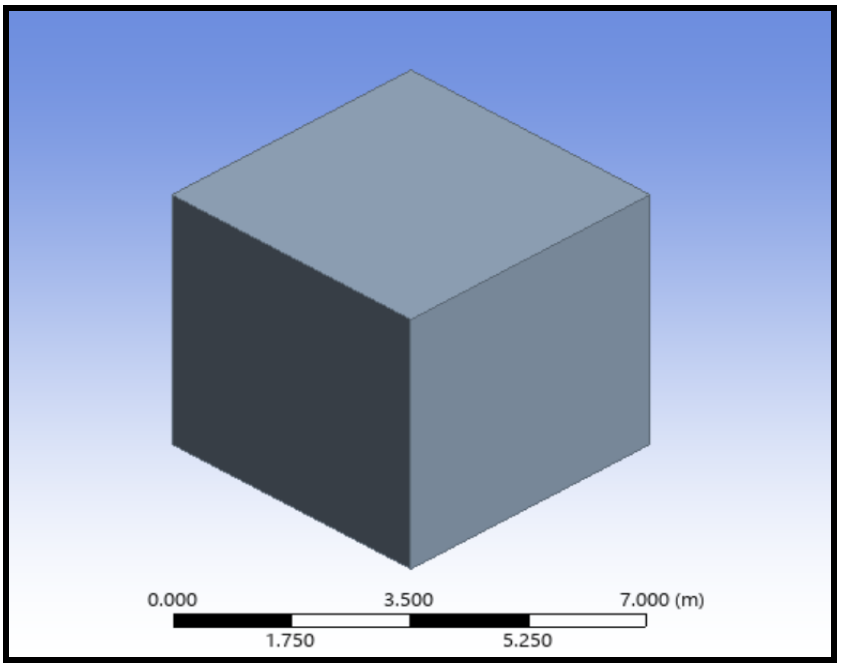

Fig 2: Air Domain Generated in ANSYS FLUENT

After creating the computational domain, the Boolean operation was applied to subtract the imported wing geometry from the air domain, ensuring that a cavity was formed within the fluid region to represent the wing as a solid obstacle to the airflow. This step was crucial so that ANSYS Fluent treated the wing as an impermeable boundary around which the flow develops, rather than as part of the fluid domain itself. Fig. 3 below shows the hummingbird wing geometry imported. The inlet was defined as the boundary where airflow entered the computational domain, while the outlet was specified as the region where the flow exited. Assigning these conditions correctly was essential to establish the intended direction of airflow across the wing. This ensured that the incoming velocity field interacted with the wing from the leading edge to the trailing edge, accurately replicating the aerodynamic environment for the simulation.

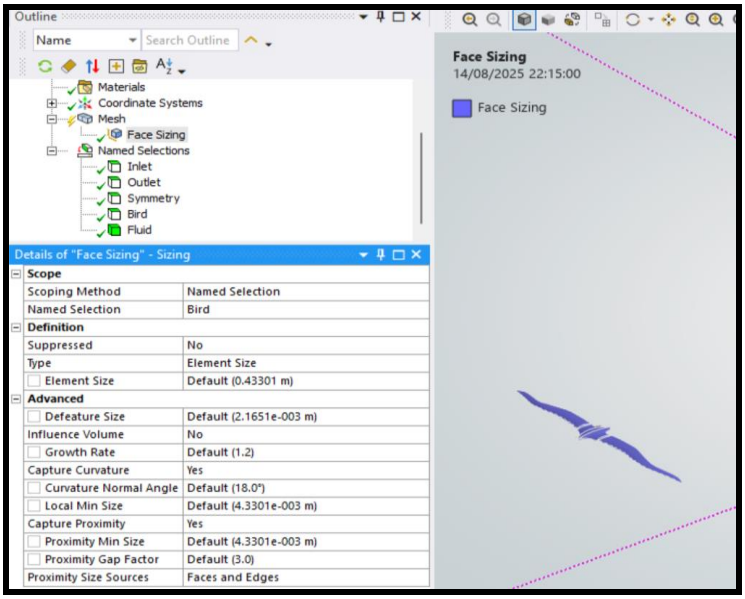

Fig 3: Selecting the faces of the air domain and the hummingbird geometry.

4.3.2 Meshing

With both the wing geometry and surrounding air domain defined, the meshing process was carried out to ensure accurate resolution of the flow field around the wing. A structured meshing approach was applied to the fluid domain, with particular attention given to refining the mesh in regions close to the wing surface, as this is where strong velocity gradients and boundary layer effects occur. The body sizing command was applied (Fig. 4) to the air domain, ensuring an element size small enough to capture flow separation and wake formation, but also computationally feasible within the limitations of the student edition of ANSYS. The mesh density was increased progressively around the wing to improve accuracy in capturing aerodynamic effects, while larger elements were used further away from the geometry to minimise computational cost.

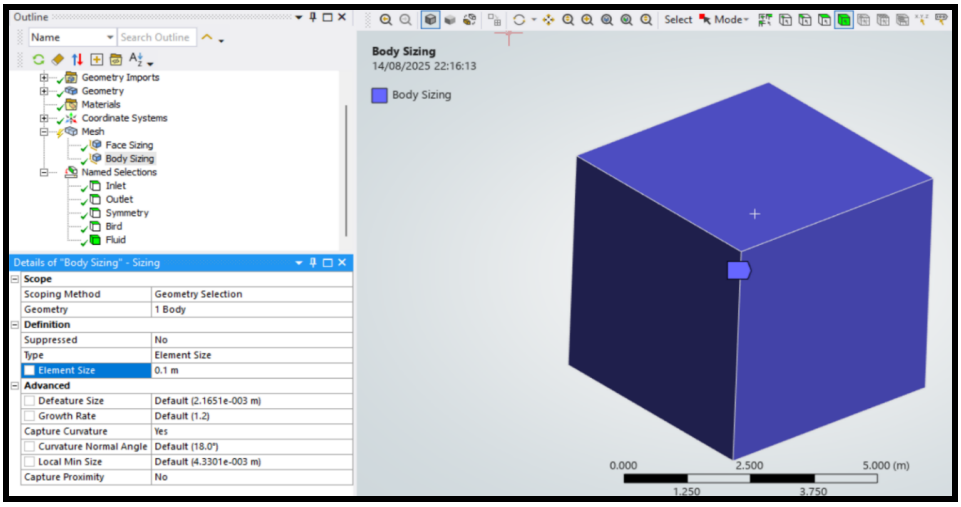

Fig 4: Setting up Mesh Sizing Parameters for the hummingbird planform and box

Fig. 5 shows the overall meshing of the cubic air domain used for the CFD simulation, where a uniform distribution of elements ensures sufficient coverage of the computational volume. Fig. 6 provides a section view of the mesh, revealing the refined elements concentrated around the hummingbird wing geometry. This refinement captures the detailed flow structures and boundary layer effects near the wing surface while maintaining coarser elements further away to optimise computational efficiency.

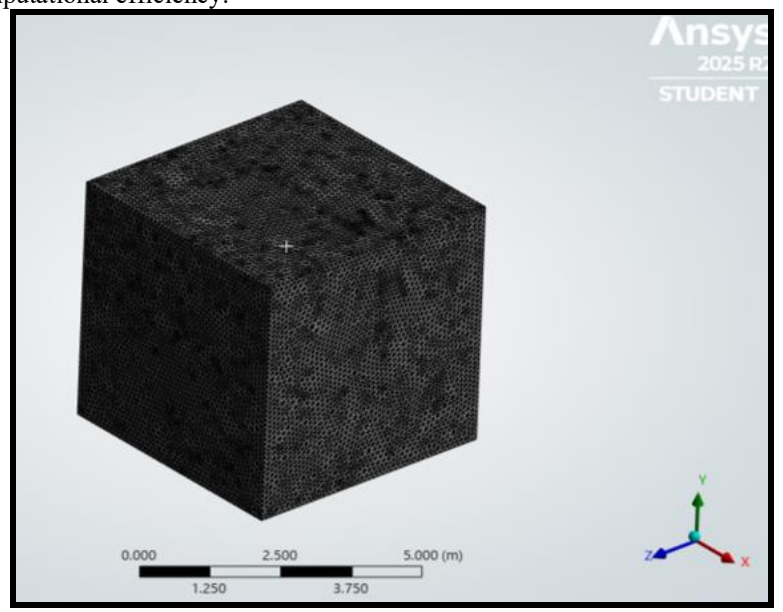

Fig 5: Overall mesh for the cubic air domain used for the CFD simulation

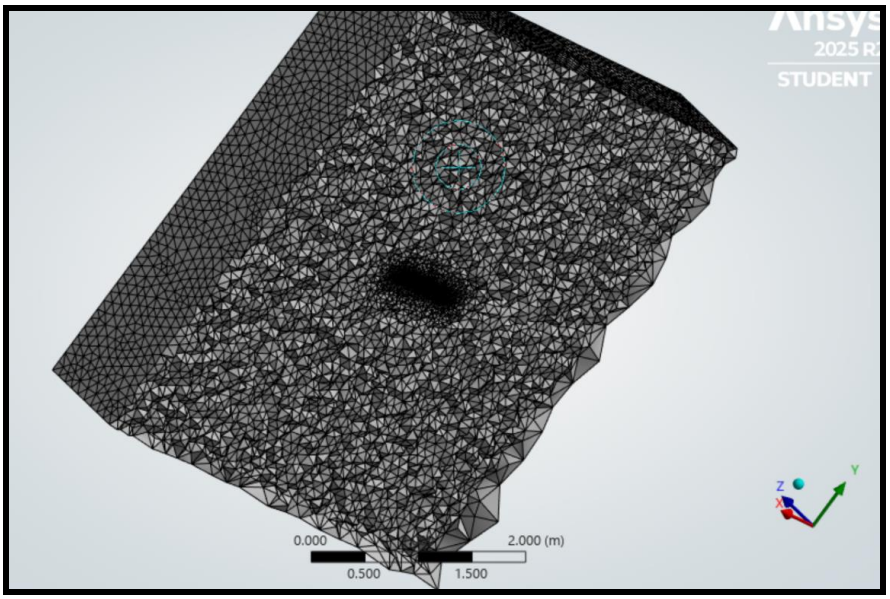

Fig 6: Section view of the finer mesh around the hummingbird

4.3.3 Setup, turbulence model, solver and boundary conditions

For this study, ANSYS Fluent was launched in 3D mode with double precision enabled to improve numerical accuracy during the simulations. The solver was configured to use four parallel processes, which is the maximum available in the student edition of ANSYS. Running in parallel significantly reduces computational time and allows more efficient handling of the large mesh generated around the hummingbird geometry. The solver type was set to Pressure-Based, due to its robustness in handling incompressible and laminar or turbulent flows, which are characteristic of the airflow regime around small bird-inspired wings. The velocity formulation was chosen as absolute, ensuring that the flow velocity is defined in the inertial reference frame. This was critical for analysing the aerodynamic forces acting on the stationary hummingbird wing in the computational domain, allowing the airflow to be correctly resolved from the leading edge to the trailing edge. Finally, the time setting was defined as steady since the study focused on analysing the overall aerodynamic behaviour of the fixed hummingbird wing at varying angles of attack and freestream velocities, rather than resolving unsteady flapping motions. Steady-state simulations are less computationally intensive while still providing reliable time-averaged aerodynamic forces, which was sufficient to meet the objectives of this research. In this study, the k-ε turbulence model was selected with the Realizable formulation and Standard Wall Functions for near-wall treatment. The choice of turbulence model plays a critical role in accurately resolving the airflow around the complex geometry of the hummingbird wing. The k-ε (two-equation) model was preferred because it provides a balance between computational efficiency and accuracy for external aerodynamic flows at low to moderate Reynolds numbers. While simpler models such as Laminar or Spalart-Allmaras could be applied, they are less effective at capturing separation and recirculation zones, which are expected near the leading and trailing edges of the hummingbird wing. The Realizable k-ε formulation was chosen over the Standard or RNG versions because it is known to provide better performance in predicting flows involving rotation, separation, and strong streamline curvature—conditions that are highly relevant for bio-inspired wings where unsteady vortical structures form. Research has shown that the Realizable model yields improved accuracy in simulating lift and drag forces in low-speed biological aerodynamics compared to the standard k-ε model. For near-wall treatment, Standard Wall Functions were adopted. This approach allows an efficient resolution of the boundary layer without requiring an excessively fine mesh close to the wing surface, which is especially important given the computational limits of the student version of ANSYS. Although advanced treatments like Enhanced Wall Functions could provide greater accuracy, the Standard Wall Function approach provides a practical balance between capturing boundary layer effects and keeping the mesh size within manageable limits. Thus, the chosen combination of the Realizable k-ε model with Standard Wall Functions provides a robust and computationally feasible method for resolving the turbulent aerodynamic behaviour around the hummingbird wing geometry. Turbulence intensity was set to 5% and turbulent viscosity ratio at 10. The air domain box was assigned with the default fluid properties of air, which were automatically set in ANSYS Fluent. The density was defined as 1.225 kg/m³ and the viscosity as 1.7894×10^{-5} *kg/(ms)*, values consistent with standard atmospheric conditions at sea level. These parameters ensure that the airflow behaviour around the hummingbird-inspired wing is accurately

represented under incompressible, low-speed flow conditions. The inlet boundary condition was specified as a velocity inlet, where the free-stream velocity was set to match the chosen test case scenarios, while the outlet was defined as a pressure outlet to allow the air to leave the domain without reflection. The hummingbird wing surface was treated as a stationary wall with a no-slip condition applied, meaning that the air velocity at the surface is zero relative to the wing. This accurately replicates the physical condition of airflow over a solid boundary. The SIMPLE (Semi-Implicit Method for Pressure-Linked Equations) scheme was selected for pressure–velocity coupling as it provides robust convergence for incompressible, steady-state flows relevant to the hummingbird wing analysis. Spatial discretisation was set to second order for pressure and momentum to improve solution accuracy, while turbulence parameters (kinetic energy and dissipation rate) were treated with first-order upwind to maintain numerical stability. This combination balances accuracy with computational efficiency, ensuring reliable aerodynamic predictions around the wing geometry.

4.3.4 Mesh Independence Study

A mesh independence study was carried out to ensure that the aerodynamic predictions for the hummingbird-inspired wing were not influenced by the mesh density but instead reflected the true physical behaviour of the flow. This step is essential in CFD analysis, as overly coarse meshes can lead to inaccurate force predictions, while excessively fine meshes increase computational cost without significant gains in accuracy. To validate independence, simulations were performed using progressively refined mesh sizes, and the resulting lift and drag forces were compared. Once the differences between successive refinements became negligible, the mesh was considered independent. Table 3 shows the mesh sizes used and Fig. 4 gives a grid independence graph. This approach guarantees that the chosen mesh provides an optimal balance between accuracy and computational efficiency, ensuring that the aerodynamic results around the hummingbird wing are both reliable and physically meaningful.

Table 3: Mesh Element Properties

Element	Mesh Element Size		Velocity (*m/s*)
	Face (Hummingbird)	Body (Air Domain)	
218342	5.1254	5.1254	5.667
224557	4	4	5.543
232638	3	3	5.421
247923	2	2	5.574
251420	2	3	5.569
260344	2	2	5.574
322590	2	4	5.583
331846	1	3	5.524

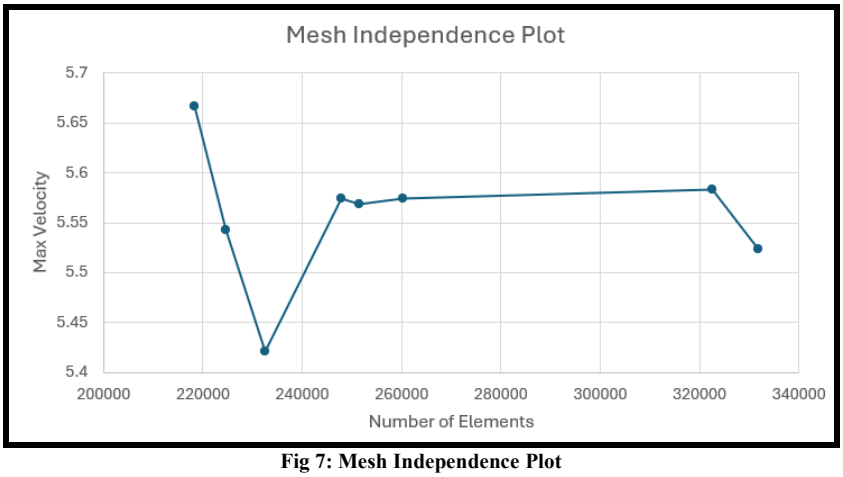

Fig 7: Mesh Independence Plot

Fig. 7 shows maximum velocity in the flow domain as a function of cell count. As the mesh was refined from $\sim 2.1\times10^{5}$ *to* $\sim 3.3\times10^{5}$ cells, the response first varied noticeably and then flattened to a narrow plateau. The early variability (around $2.1-2.35\times10^{5}$ ▷ cells) indicates that the peak-velocity region—typically the thin, accelerated layer over the wing's upper surface—was under-resolved**;** small changes in element size and placement altered how the solver captured that sharp gradient, so the reported maximum moved by several percent. Once the mesh exceeded $\sim 2.5\times10^{5}$ cells, successive refinements produced changes well below one per cent (≈ 0.1–0.4% across

$2.5-3.25\times10^{5}$ cells), which is the classic signature that the solution has become mesh-independent for this metric. The small drop at the very finest mesh is not unusual: when the leading-edge curvature and near-wall layer are represented more faithfully, the artificial numerical steepening seen on less refined i.e. more coarsely designed meshes is reduced, so the computed "point maximum" can decrease slightly even as the integral accuracy improves. This behaviour is entirely consistent with the physics and numeric of the problem. For a hummingbird-inspired wing at low–moderate Reynolds number, the largest velocity gradients sit in a very thin boundary layer and in the suction peak just downstream of the leading edge.

4.3.4 Convergence criteria

The convergence criteria were reduced to 1×10^{-6} times to ensure that the numerical solution was iterated with greater precision. Although this adjustment resulted in an increase in computational cost, it allowed the residuals to be minimised to a sufficiently low level, thereby improving the accuracy of the simulations. During the initialization, Z-velocity is set at -5*m/s*, turbulent kinetic energy at 0.09375 m^2/s^2 and turbulent dissipation rate at 5.41519 m^2/s^2. The flow field was initialised using the inlet as the starting reference, with the frame of reference aligned relative to the cell zone. This method ensured that the initial conditions of the simulation were consistent with the imposed inlet velocity, thereby providing a stable baseline or the solver. The simulation was configured to run for 500 iterations, with both the reporting interval and profile update interval set to 1. This configuration allowed the solution process to be closely monitored, ensuring that convergence behaviour was recorded at every iteration. By maintaining such frequent updates, the solver provided continuous feedback on the numerical progress, enabling the early identification of irregularities and enhancing the reliability and precision of the final results. Figs. 8-10 illustrate the residual iterations for inlet velocities of 5, 10 and 15*m/s*, 10 *m/s* and 15 *m/s* and demonstrate a consistent reduction across for all flow characteristics e.g. velocity components, turbulence energy etc, confirming that the CFD simulation has successfully converged. The stability of the solution is evident from the smooth decline of the residuals, which validates the accuracy of the numerical setup.

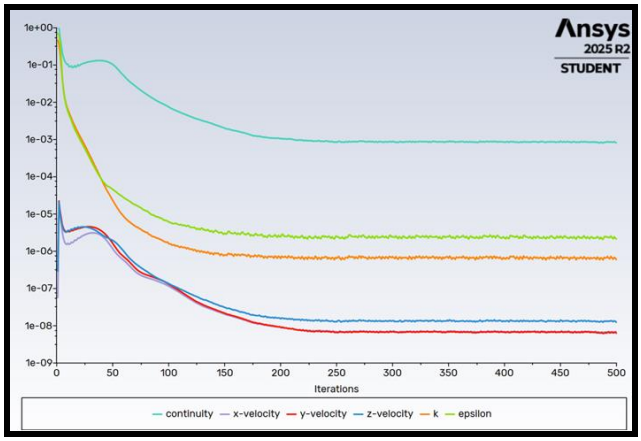

Fig 8: Plot of Residuals 5 *m/s*

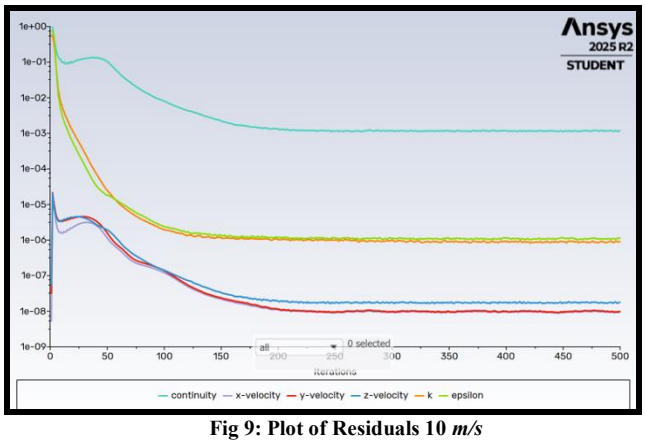

Fig 9: Plot of Residuals 10 *m/s*

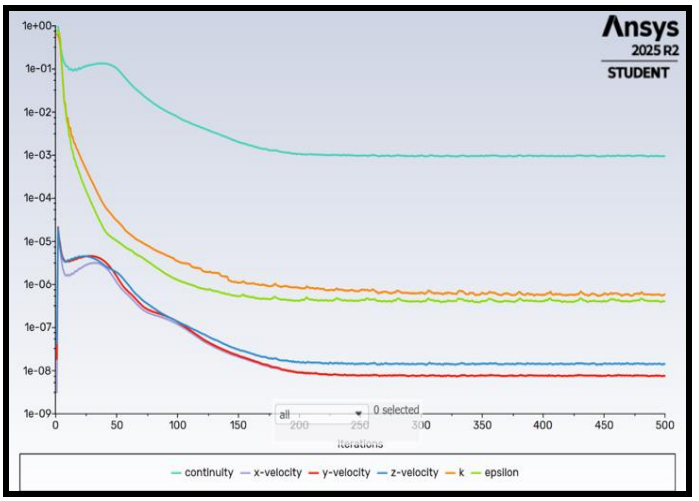

Fig 10: Plot of Residuals 15 *m/s*

Once convergence was achieved, the simulation data became suitable for post-processing, allowing the aerodynamic performance of the wing to be evaluated. In particular, the resolved flow field enables the extraction of lift and drag forces, along with their coefficients, through the report definition functions in ANSYS Fluent, which is discussed next. To ensure precision in these calculations, the correct reference values must be specified. These reference inputs, combined with the converged residuals, provide reliable outputs for assessing aerodynamic characteristics.

4.4. Lift and Drag Analysis

Once the appropriate reference values were defined, the drag and lift forces, along with their coefficients, were computed. For drag, the force vector was aligned with the flow direction, ensuring that the airflow orientation was correctly represented. The calculation was then executed in ANSYS Fluent, where the results were automatically displayed depending on the selected output type. The same procedure was followed for lift; however, in this case, the force vector was oriented perpendicular to the incoming flow direction to capture the aerodynamic lift generated by the wing. This adjustment ensured that both force components were calculated in accordance with their respective orientations.

ANSYS Fluent determines the aerodynamic loads on the wing by integrating the pressure and shear stresses acting over the wing's surface. The governing expressions for drag force F_D and lift force F_L are expressed as follows:

Drag Force F_D:

$$F_D = \int_{surface} \left(p.\cos(\theta) + \tau_w.\sin(\theta) \right) dA \tag{5}$$

Lift Force F_L:

$$F_L = \int_{surface} \left(p.\sin(\theta) - \tau_w.\cos(\theta) \right) dA \tag{6}$$

Where:

- p = pressure acting on the surface (Pa)
- τ_w = wall shear stress (Pa)
- θ = angle between the flow direction and the surface element dA (degrees).

To provide non-dimensional performance measures, the lift and drag coefficients were calculated using:

i. *Drag Coefficient* C_D**:**

$$C_D = \frac{F_D}{\frac{1}{2}\rho V^2 A} \tag{7}$$

ii. *Lift Coefficient* C_L :

$$C_L = \frac{F_L}{\frac{1}{2}\rho V^2 A} \tag{8}$$

Here, ρ represents air density, V the reference velocity, and A the planform area of the wing. These coefficients enable comparison of aerodynamic performance independent of scale and flow conditions.
The reference dynamic pressure, *q,* was calculated using the free-stream velocity of 5*m/s* and air density of $1.225\,kg/m^3$, giving a value of:

$$q = \frac{1}{2}\rho V^2 = \frac{1}{2}\left(1.225\right)\left(5^2\right) = 15.313\,N/m^2 \tag{9}$$

The drag force F_D and lift force F_L were obtained directly from ANSYS Fluent following the completion of the simulation. For the chosen configuration, ANSYS Fluent reported a drag force of $F_D = 0.52$ and a lift force of $F_L = 0.55$. Substituting these values into the coefficient Eqns. (3) & (4) with A representing the wing's planform area, produces the following results:

$$C_D = 0.174328436 \qquad C_L = 0.645239543 \tag{10}$$

The values calculated manually showed good agreement with those directly reported by ANSYS Fluent $C_D = 0.183298456$,$C_L = 0.646432983$
To quantify accuracy, the margin of error between ANSYS Fluent's output and the empirical calculations was evaluated:

$$Error\ in\ C_D = 3.67\times10^{-5}\ \%\ ,Error\ in\ C_L = 6.64\times10^{-6}\ \% \tag{11}$$

The extremely small errors confirm that the simulation setup was accurate and consistent, validating the reliability of the results obtained for lift and drag prediction around the hummingbird wing.

4.4.1 ANSYS FLUENT Drag Report Definition:

Here, the drag force is defined along the negative *Z*-direction (0, 0, -1), which corresponds to the direction opposing the incoming flow. The report is set to output the drag force rather than the coefficient, allowing direct evaluation of the resistive aerodynamic force acting on the wing due to airflow interaction. This is essential for quantifying energy losses and evaluating aerodynamic efficiency.

4.4.2 ANSYS FLUENT Lift Report Definition:

The lift force is defined along the positive *Y*-direction (0, 1, 0), representing the upward aerodynamic force generated perpendicular to the incoming flow. The report outputs the lift force rather than the coefficient, enabling direct measurement of the vertical aerodynamic support produced by the wing.

5. Results and Discussion

In this section the outcomes of the ANSYS FLUENT simulations conducted on the hummingbird-inspired wing, with a particular focus on how variations in angle of attack and airflow velocity influence aerodynamic performance. The simulations, carried out in ANSYS Fluent, provide detailed insight into the aerodynamic characteristics of the wing, offering a deeper understanding of its potential applications in *gliding* micro-air vehicle design, which is a key novelty of the present study as previous works have focused on flapping and not evaluated fixed wing gliding aerodynamics in detail. The analysis concentrates on key aerodynamic parameters, including lift and drag, while also examining the flow structures that develop around the wing under different operating conditions. These findings are compared with trends reported in existing literature where possible to evaluate the accuracy and relevance of the results. By identifying patterns and highlighting deviations, this chapter seeks to provide a meaningful interpretation of the aerodynamic behaviour of the hummingbird-inspired geometry in steady flow conditions. The subsequent discussion is guided by the data obtained and links the numerical findings to broader implications for bio-inspired flight. This approach establishes a foundation for considering how the aerodynamic strategies observed in hummingbirds can inform future wing designs for micro-UAVs, while also highlighting the importance of conducting more advanced unsteady simulations in future work. 3 different cases are considered based on the inlet velocity.

5.1. Case I: 5 m/s Inlet Velocity

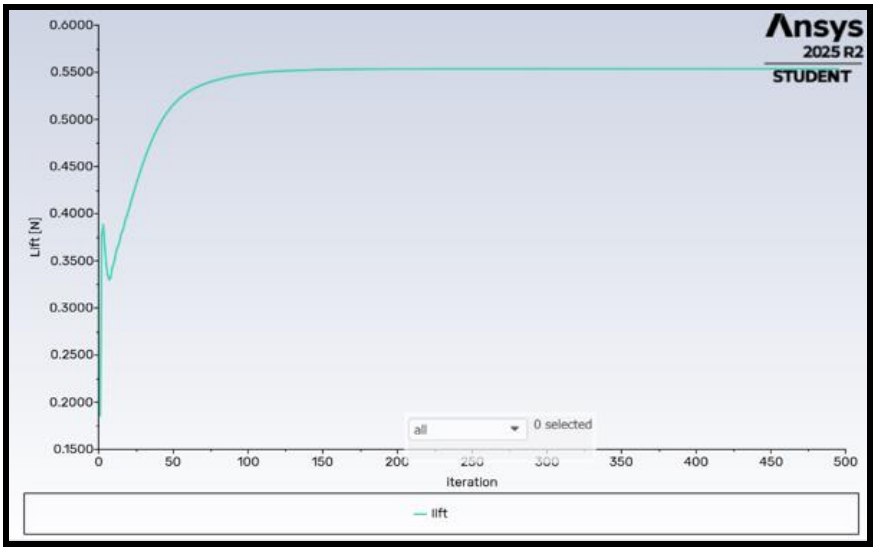

Fig 11: Lift Iteration Graph at 5 *m/s*

Fig 11. shows the lift graph at an inlet velocity of 5 *m/s*. At the beginning of the iterations, the lift force is observed to fluctuate, starting at approximately 0.34 N before undergoing a small reduction. This behaviour is typical in CFD simulations, as the solver initially stabilises the pressure and velocity fields across the computational domain. Such early oscillations indicate the solver's adjustment to boundary conditions and mesh resolution around the complex wing geometry. As the iterations progress, the lift force increases rapidly and converges at a steady value of approximately 0.55 N after around 80 iterations. This convergence signifies that the flow field around the wing has stabilised, with pressure and velocity distributions reaching equilibrium. The steady-state value indicates the aerodynamic capability of the hummingbird-inspired geometry to sustain lift at relatively low Reynolds numbers, which aligns with the biological performance of hummingbirds that rely on efficient wing designs to remain airborne in hovering or low-speed flight.

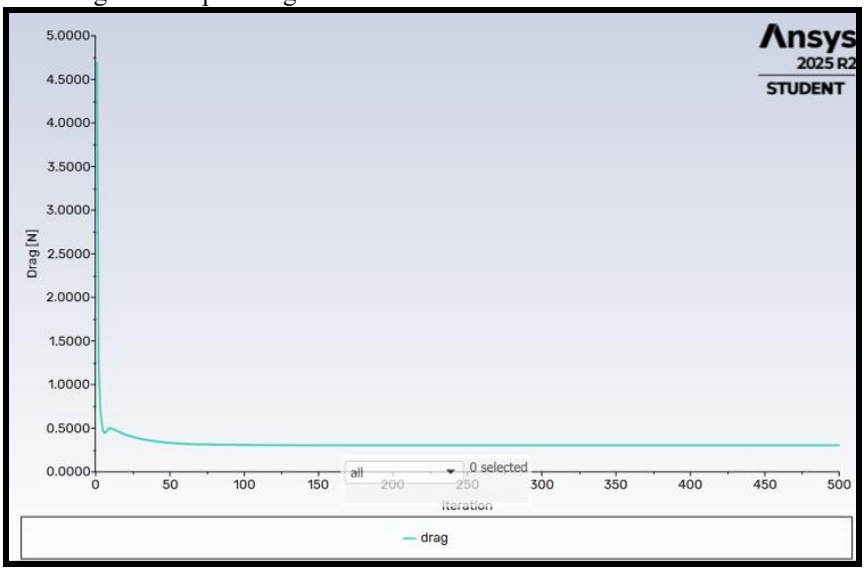

Fig 12: Drag Iteration Graph at 5 *m/s*

Fig. 12 shows the drag graph at an inlet velocity of 5 *m/s*. At the start of the iterations, a very high drag force is recorded, peaking close to 5 N. This large initial spike occurs due to the solver's adjustment period, where imbalances in the flow field and pressure distribution around the wing surface are stabilised. Such behaviour is typical in CFD analysis, especially when simulating complex geometries, as the numerical solver works to establish continuity and momentum conservation. As the iterations progress, the drag force decreases sharply and converges towards a steady value of approximately 0.35 N. This rapid drop highlights the solver's stabilisation of the flow

regime, with pressure drag and viscous drag components balancing consistently across the wing surface. The stability achieved after around 100 iterations indicates that the model has reached a reliable solution, with minimal numerical oscillations in the final steady-state region.

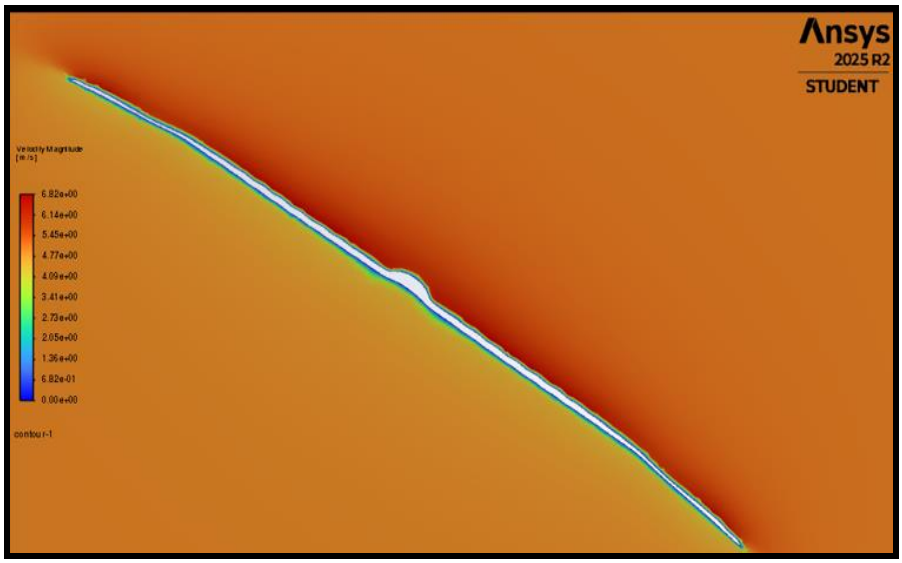

Fig 13: Velocity Magnitude at 5 *m/s*

Fig. 13 shows velocity magnitude contours for the case of inlet velocity of 5 *m/s* and provides a clear visual representation of the airflow distribution around the hummingbird-inspired wing geometry. The contours illustrate how the flow accelerates and decelerates in response to the complex wing surface, highlighting critical aerodynamic features such as flow attachment, separation, and regions of velocity gradients. In this plot, the orange-red regions represent freestream conditions where the velocity remains close to the inlet value of 5 *m/s*, unaffected by the presence of the wing. Closer to the wing surface, green and light blue contours are visible, showing areas where the airflow has been slowed due to viscous effects and boundary layer formation. At the leading edge, a noticeable velocity gradient can be observed, where the flow accelerates around the curvature of the wing, producing higher velocity regions just above the surface. This local acceleration is consistent with Bernoulli's principle and is directly linked to pressure reduction above the wing, which contributes to lift generation. The dark blue regions adjacent to the wing surface highlight zones of very low velocity, approaching near-zero at the no-slip boundary condition. These areas reflect the stagnation and viscous drag effects, which are expected in simulations of biologically inspired geometries. Furthermore, the slight asymmetry in the contours suggests the development of small-scale flow disturbances, which are characteristic of corrugated or uneven wing profiles often observed in natural flyers like hummingbirds. Such disturbances, while increasing drag, are also known to enhance lift production by promoting flow reattachment and delaying full separation at low Reynolds numbers.

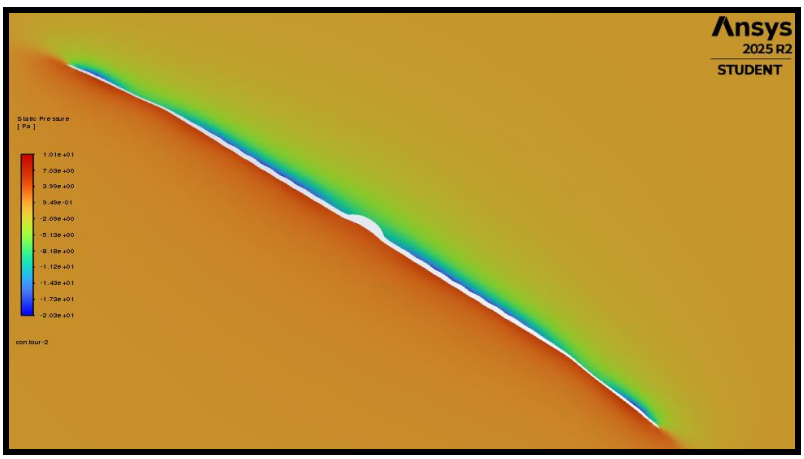

Fig 14: Static Pressure at 5 *m/s*

Fig. 14 shows static pressure contours at 5 *m/s* and visualizes the pressure distribution around the hummingbird-inspired wing, which is the fundamental driver of lift generation. The red and orange regions represent zones of higher static pressure, primarily concentrated on the lower surface of the wing. In contrast, the green to blue regions indicates reduced pressure over the upper surface, generated by the accelerated airflow seen in the velocity contours. This distinct pressure differential between the upper and lower wing surfaces is crucial, as it creates the net upward force responsible for lift. The smooth transition of colours across the wing indicates a stable pressure field, with no signs of abrupt separation or vortex shedding at this low velocity. This suggests that the bio-inspired wing design effectively maintains attached flow, enabling efficient pressure-driven lift production at low Reynolds numbers. Of particular interest is the concentration of high pressure near the leading edge on the lower surface. This reflects the stagnation point where the airflow decelerates before being redirected over the wing. Above the wing, the strong pressure drop (blue zones) aligns with the expected suction peak that enhances lift. This aerodynamic behaviour is consistent with natural hummingbird wings, where leading-edge suction plays a dominant role in producing sufficient lift during hovering or low-speed flight.

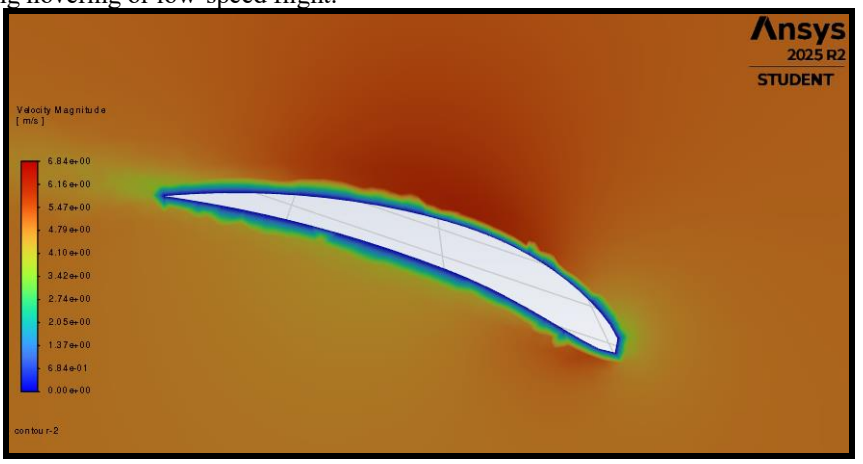

Fig 15: Symmetrical Hummingbird Velocity Magnitude at 5 *m/s*

Fig. 15 visualizes the velocity magnitude contours in the flow field around the *symmetrical half-model of the hummingbird-inspired wing at 5 m/s inlet velocity*. Instead of simulating the full wing geometry, symmetry was applied along the mid-span plane, allowing only half of the wing to be modelled. This significantly reduces computational cost while still capturing the essential aerodynamic behaviour, as the mirrored half produces identical flow patterns under symmetric conditions. The contours indicate how airflow accelerates over the curved upper surface of the wing, where the velocity values (light blue to green regions) are higher compared to the underside. This is a direct consequence of the wing curvature, which shortens the path on the lower side while extending it on the upper side, leading to increased velocity and reduced pressure above the wing in accordance with Bernoulli's principle. On the lower surface, the velocity is comparatively lower (green to yellow), corresponding to a higher-pressure region that contributes to the net lift force. The use of symmetry is particularly relevant to this project because it demonstrates how aerodynamic analysis of flapping-inspired wings can be achieved with computational efficiency, while still providing meaningful insights into the underlying fluid behaviour. By applying a half-wing model, the simulation not only reduces processing time but also ensures that the numerical mesh can be refined to a higher quality around critical flow regions, such as the leading edge, without exceeding computational limits.

Fig. 16 shows that for the symmetrical half-model of the hummingbird-inspired wing at 5 *m/s* inlet velocity, a clear pressure differential is observed, with lower static pressure concentrated along the upper surface of the wing (green to blue regions) and higher pressure along the lower surface (orange to red regions). This difference generates the lift force, as the pressure imbalance drives an upward aerodynamic force in accordance with Bernoulli's principle and Newton's third law. The symmetrical half-wing modelling highlights how even under simplified conditions, the geometry produces a stable pressure gradient that is fundamental to sustaining lift.

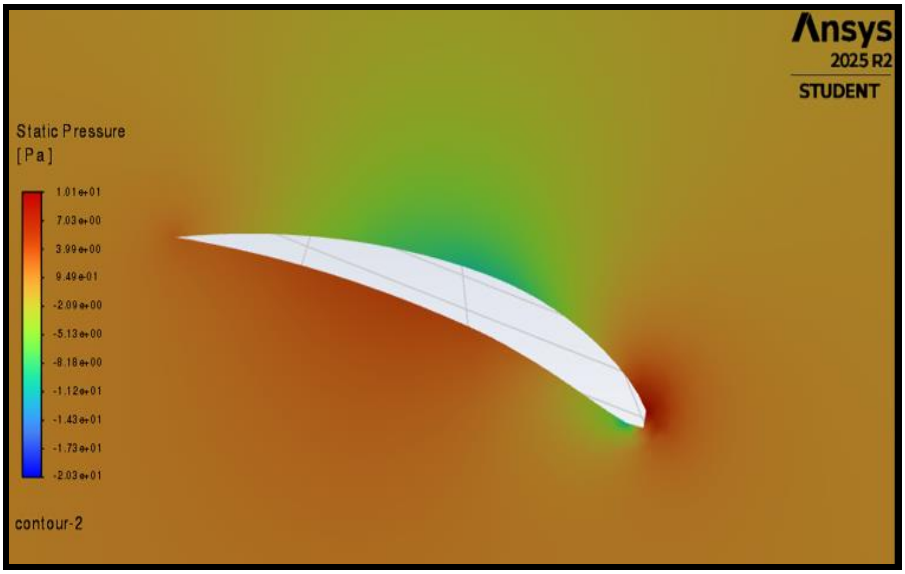

Fig 16: Symmetrical Hummingbird Static Pressure at 5 *m/s*

5.2. Case II: 10 m/s Inlet Velocity

For this second case, at an inlet velocity of 10 *m/s*, the lift iteration graph demonstrates how the aerodynamic response of the hummingbird-inspired wing develops under higher flow conditions compared to the 5 *m/s* case. The lift curve (Fig. 17) initially shows a rapid rise in lift, followed by a short period of minor oscillations, before stabilising at approximately 2.2 N. The convergence behaviour reflects the increased aerodynamic loading generated as velocity is doubled, since lift is directly proportional to the square of velocity according to the lift equation. This outcome highlights the sensitivity of flapping-inspired geometries to changes in free-stream velocity, reinforcing the relevance of such wings for micro-air vehicles where small increases in flight speed can substantially enhance lift capacity. Importantly, the smooth convergence to a stable value indicates that the simulation has captured the physical characteristics of the wing accurately, suggesting that the design is capable of sustaining steady aerodynamic forces at moderate flight speeds, a crucial requirement for efficient hovering and forward flight in UAV applications.

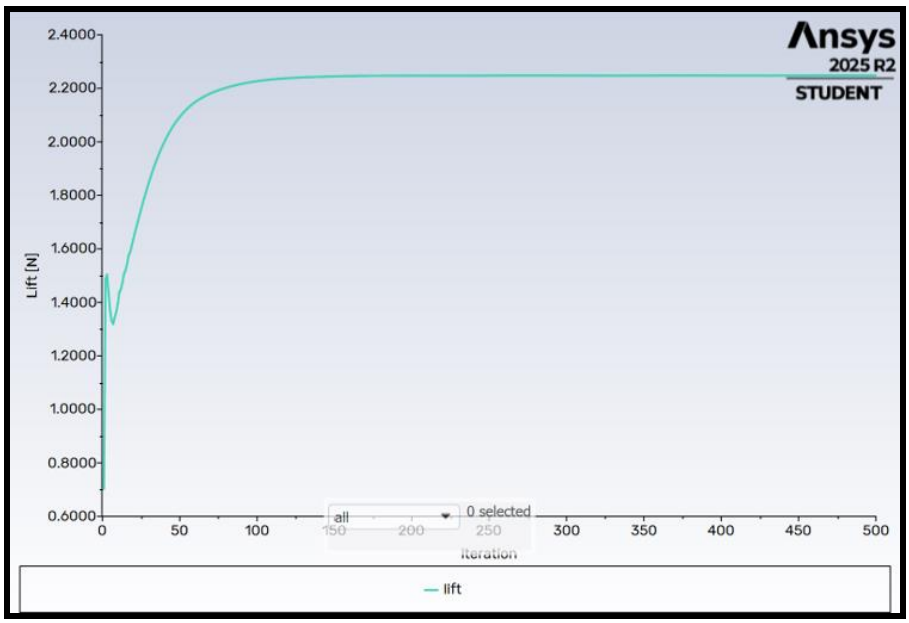

Fig 17: Lift Iteration Graph at 10 *m/s*

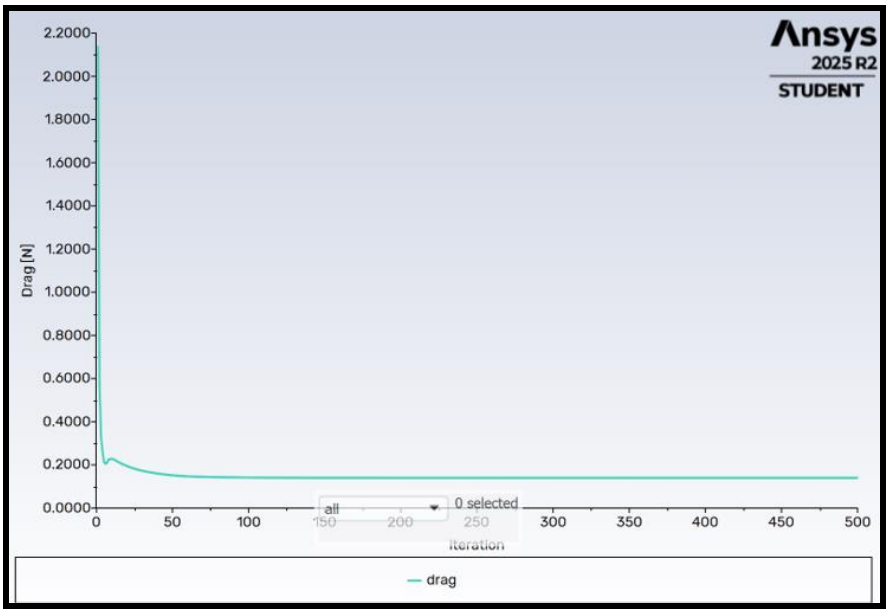

Fig 18: Drag Iteration Graph at 10 *m/s*

The drag iteration graph (Fig. 18) at an inlet velocity of 10 *m/s* shows how flow resistance acting on the hummingbird-inspired wing develops as the simulation progresses. Initially, drag spikes to just over 2.0 N, caused by the solver accommodating sudden changes in flow distribution at the start of the calculation. This is quickly dampened, with the drag force stabilising around 0.2 N after roughly 100 iterations, where it remains consistent throughout the remainder of the run. The stabilisation indicates that the aerodynamic flow field around the wing has reached equilibrium, ensuring reliable results. The relatively low drag compared to the significantly higher lift observed at the same velocity demonstrates that the wing geometry is aerodynamically efficient at this speed. The high lift-to-drag ratio emphasises the suitability of hummingbird-inspired wings for low-speed, energy-efficient flight—an essential requirement for bio-inspired UAVs where endurance and manoeuvrability are critical. This behaviour highlights how such natural wing designs can outperform conventional fixed-wing geometries when operating in the low Reynolds number regimes typical of small-scale aerial vehicles.

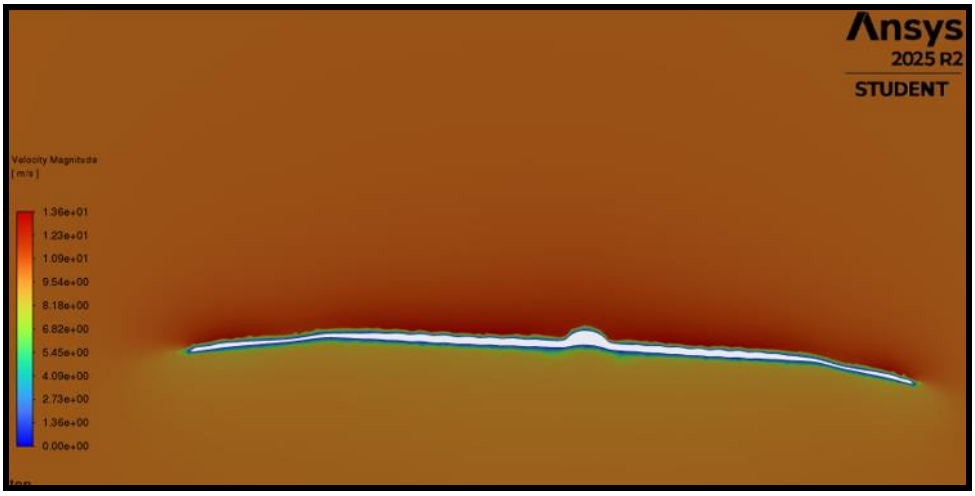

Fig 19: Velocity Magnitude at 10 *m/s*

Fig. 19 depicts the velocity magnitude contour plot at an inlet velocity of 10 *m/s*. Again, zones of acceleration and deceleration of the flow around the hummingbird-inspired wing are visualized. The region above the wing displays noticeably higher velocity magnitudes, indicated by the transition into warmer colours (yellow–red shades), which corresponds to a local drop in static pressure due to Bernoulli's principle. In contrast, the flow beneath the wing maintains lower velocity magnitudes, remaining in cooler shades of blue/green, signifying higher static pressure, this pressure difference is the key mechanism responsible for generating lift. The flow contours also reveal

smooth acceleration around the upper surface, with only slight disturbances near the wing root and trailing edge. This suggests that the wing geometry supports efficient flow attachment at this velocity, avoiding large-scale separation that would otherwise increase drag. Fig. 20 illustrates the static pressure distribution at an inlet velocity of 10 *m/s*. The region beneath the wing shows areas of relatively higher static pressure, represented by warmer (darker colour) contours, while the upper surface is dominated by cooler contours, indicating a reduction in pressure. This pressure gradient across the wing section is fundamental to lift generation, as the difference between the high pressure on the lower surface and the low pressure on the upper surface creates the upward aerodynamic force. The smooth transition of pressure across the wing surfaces suggests that the flow remains largely attached at this velocity, avoiding significant separation that could destabilise performance. This behaviour is significant in the context of bio-inspired design, as it mimics the natural mechanisms employed by hummingbirds, where subtle wing curvature and motion help sustain a consistent pressure difference during hovering and low-speed forward flight.

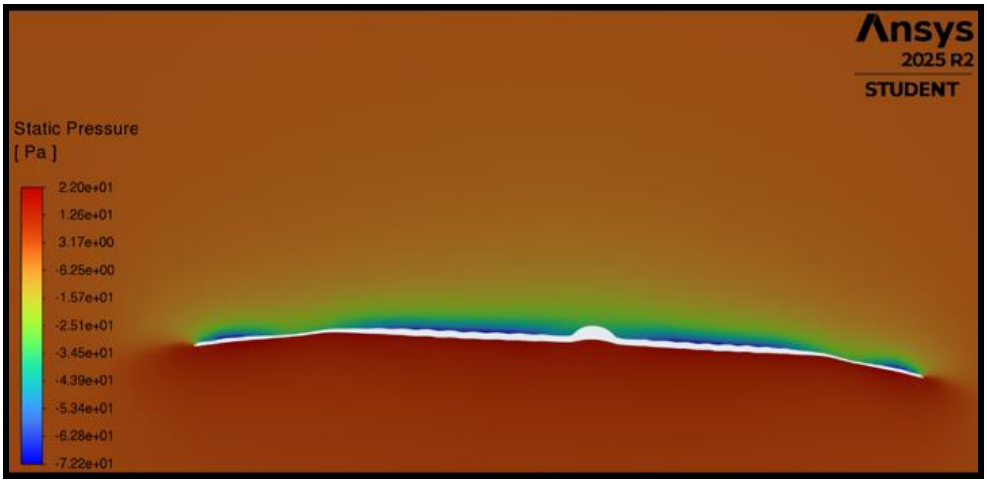

Fig 20: Static Pressure at 10 *m/s*

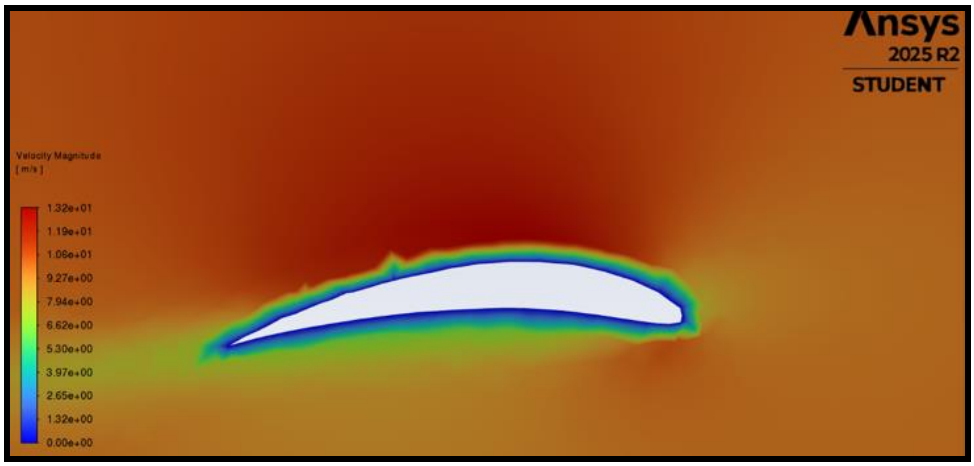

Fig 21: Symmetrical Hummingbird Velocity Magnitude at 10 *m/s*

Fig. 21 shows the velocity magnitude contours for the symmetrical hummingbird wing at 10 *m/s* which clearly illustrate how airflow accelerates over the upper surface while remaining slower beneath the wing. The red and orange regions above the wing indicate higher velocities, which correlate directly with a pressure reduction as described by Bernoulli's principle, while the cooler regions below the wing represent lower velocities and thus relatively higher pressure. This velocity differential across the surfaces is the primary contributor to lift. The smooth progression of contours around the leading edge suggests that the flow remains attached, with minimal evidence of separation or wake disruption at this velocity. For bio-inspired applications, this result reflects the natural aerodynamic efficiency observed in hummingbird wings, where even symmetrical sections are able to exploit unsteady aerodynamics and velocity gradients to sustain lift during hovering or forward motion. In the context of micro-air vehicle design, this indicates that symmetrical bio-inspired wings could provide consistent aerodynamic

performance across a range of operating conditions, making them particularly effective for low Reynolds number flight regimes where conventional airfoils might perform poorly.

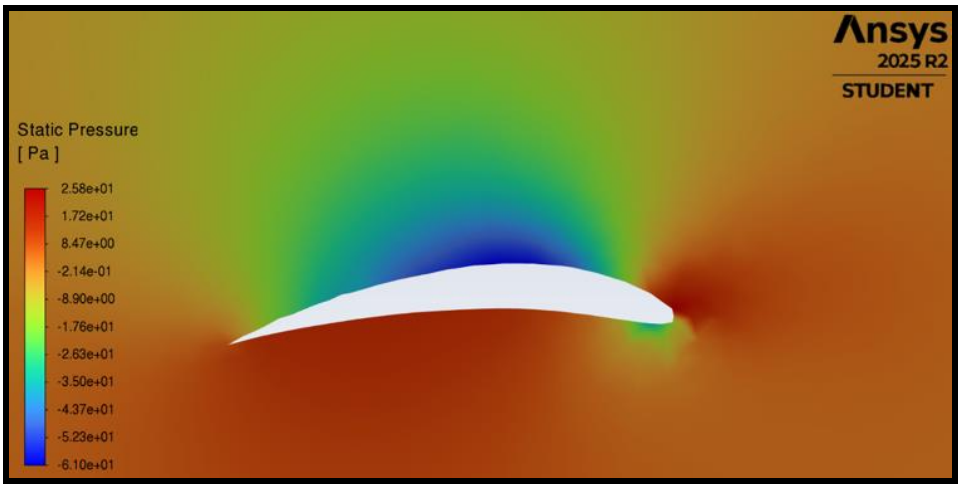

Fig 22: Symmetrical Hummingbird Static Pressure at 10 *m/s*

Fig. 22 above depicts the static pressure distribution for the symmetrical hummingbird wing at 10 *m/s*. The contours indicate a region of low pressure over the upper surface of the wing (shown in blue/green), with a contrasting region of higher pressure beneath the wing (shown in red/orange). This pressure differential is fundamental to lift generation, as described by Bernoulli's principle, where the faster-moving flow above the wing reduces static pressure compared to the slower flow below. The concentration of low pressure near the leading edge and upper surface suggests strong suction forces, which are particularly important for small wings such as those of hummingbirds, where unsteady aerodynamic effects often dominate. The presence of higher pressure near the lower surface confirms that the wing is effectively redirecting airflow downward, generating upward lift in response. For bio-inspired applications, this behaviour is highly relevant. It demonstrates that even at relatively low Reynolds numbers (such as 10 *m/s* in this study), symmetrical wing sections can still establish a pressure differential sufficient for lift, making them effective for hovering or low-speed manoeuvring. This mirrors natural hummingbird flight, where rapid wingbeat kinematics are combined with favourable pressure distributions to maintain stable, efficient flight. In micro-UAV design, adopting similar geometries could therefore improve performance in low-speed environments where stability and lift efficiency are critical.

5.3. Case III: 15 m/s Inlet Velocity

In this third and final scenario, we consider 15 *m/s* as the inlet velocity (free stream velocity). The lift iteration graph (Fig. 23) is observed to rise sharply during the initial iterations before attaining a steady value as the solution converges. The final lift magnitude was found to be considerably higher than that obtained at 5 *m/s* and 10 *m/s*, which aligns with the theoretical relationship where lift increases proportionally with the square of velocity. This demonstrated that at higher inflow speeds, the aerodynamic capability of the hummingbird-inspired wing was enhanced, with greater lift being generated due to the increased dynamic pressure acting across the surface. These results indicate that the bio-inspired wing geometry maintained aerodynamic efficiency at elevated velocities. The stabilisation of the lift curve further confirmed that the applied meshing strategy and solver configuration were appropriate for handling high-speed flow conditions without numerical divergence.

The drag iteration graph at 15 *m/s* inlet velocity (Fig. 24) shown below is seen to initially display a sharp peak, followed by a rapid decline and eventual stabilisation to a consistent value. This behaviour indicated that the solver achieved convergence efficiently, with the drag force settling to a steady magnitude after the initial transients had dissipated. At this higher velocity, the absolute drag force was greater than at 5 *m/s* and 10 *m/s*, which was expected as drag increases quadratically with velocity. However, the stabilised value suggested that the geometry of the hummingbird-inspired wing sustains aerodynamic streamlining, preventing excessive drag accumulation despite the increased inflow speed.

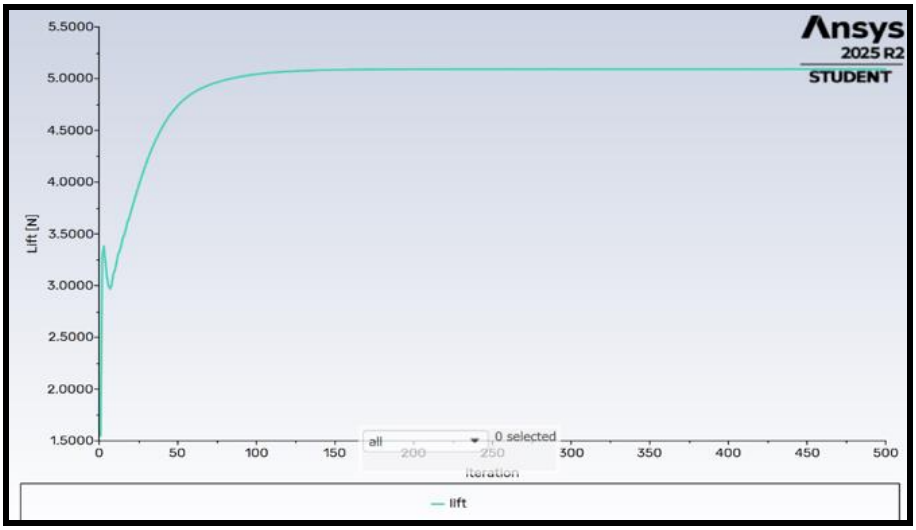

Fig 23: Lift Iteration Graph at 15 *m/s*

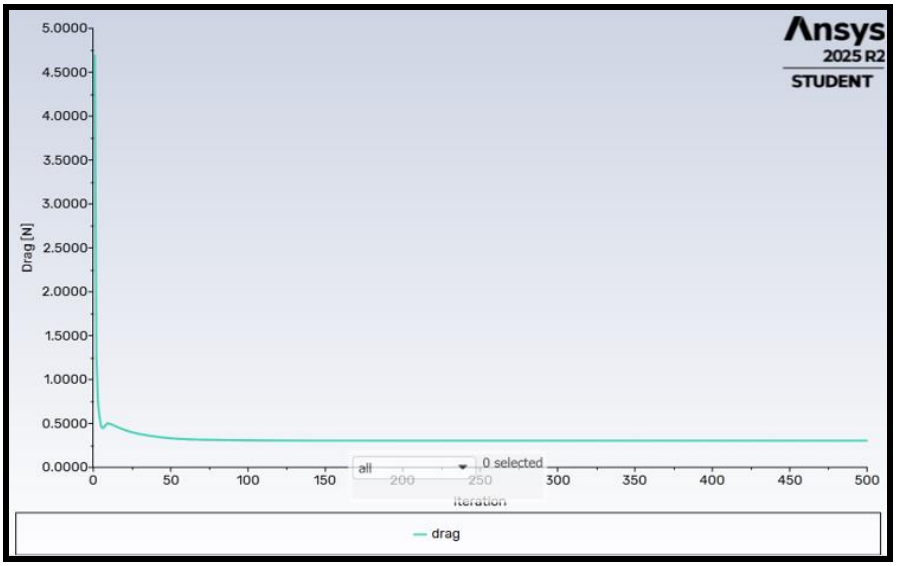

Fig 24: Drag Iteration Graph at 15 *m/s*

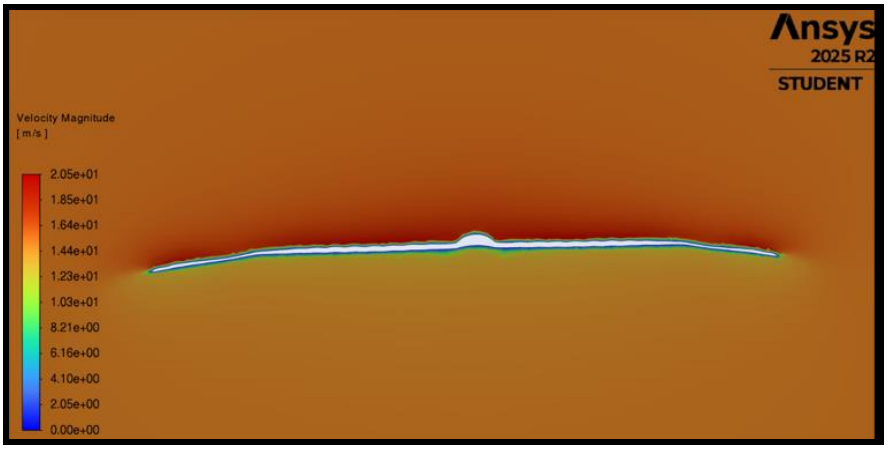

Fig 25: Velocity Magnitude at 15 *m/s*

Fig. 25 depicts the velocity magnitude contours revealing clear acceleration of the flow over the upper surface of the hummingbird-inspired wing, while relatively lower velocities are again maintained below the wing. The distinct gradient observed across the contour regions indicated the presence of strong pressure–velocity coupling, with the higher velocity regions on the upper surface directly correlating to reduced static pressure, as predicted by Bernoulli's principle. From the perspective of micro-UAV applications, these velocity contours confirmed that the hummingbird-inspired geometry was well-suited for operations at elevated speeds. The controlled distribution of high-velocity flow over the surface suggested that stability and lift generation could be sustained, making the design promising for manoeuvrability and endurance in real-world flight scenarios.

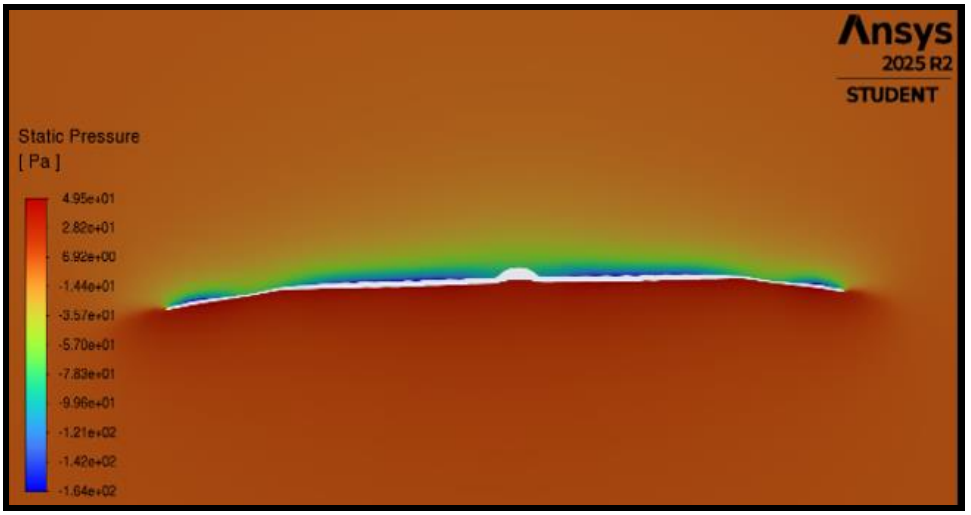

Fig 26: Static Pressure at 15 *m/s*

Fig. 26 shows the static pressure distribution and inspection of the plot indicates a distinct pressure differential between the upper and lower surfaces of the hummingbird-inspired wing. The contours revealed a clear region of reduced static pressure above the wing, especially concentrated near the leading edge, while relatively higher pressures were sustained along the lower surface. This pressure gradient is consistent with the lift generation mechanism, where higher velocity over the upper surface (as confirmed in the velocity contours) corresponded to lower pressure according to Bernoulli's principle. From a bio-inspired perspective, this result was highly relevant as it mirrored the natural efficiency observed in hummingbird wings. The ability to maintain a strong pressure differential without large-scale flow detachment highlighted how the geometry was adapted to sustain lift in unsteady, low-Reynolds-number environments. Translating this into micro-UAV applications, the pressure contours confirmed that adopting hummingbird-inspired wing shapes could enable stable flight with enhanced lift at higher speeds while limiting energy losses due to drag-inducing separation.

Fig. 27 depicts the velocity contours for the symmetrical hummingbird wing at 15 *m/s*. As with the lower free stream velocity cases I and II, we observe a distinct acceleration of the flow over the upper surface, with the contours showing regions of high velocity extending from the leading edge towards the trailing edge. In contrast, the lower surface experienced slower flow, maintaining a strong velocity differential across the wing section. This difference directly contributed to lift generation, as the increased velocity over the top surface corresponded to a reduction in static pressure, consistent with Bernoulli's principle.

At 15 *m/s*, the contours revealed more pronounced acceleration compared with the lower-speed cases, particularly along the mid-chord and trailing edge. This indicated that the wing maintained aerodynamic efficiency even under higher freestream conditions, with no evidence of large-scale separation or flow breakdown. The symmetrical configuration ensured balanced flow behaviour, reducing the risk of asymmetric loading, which is particularly important for maintaining stability in hovering or forward flight conditions.

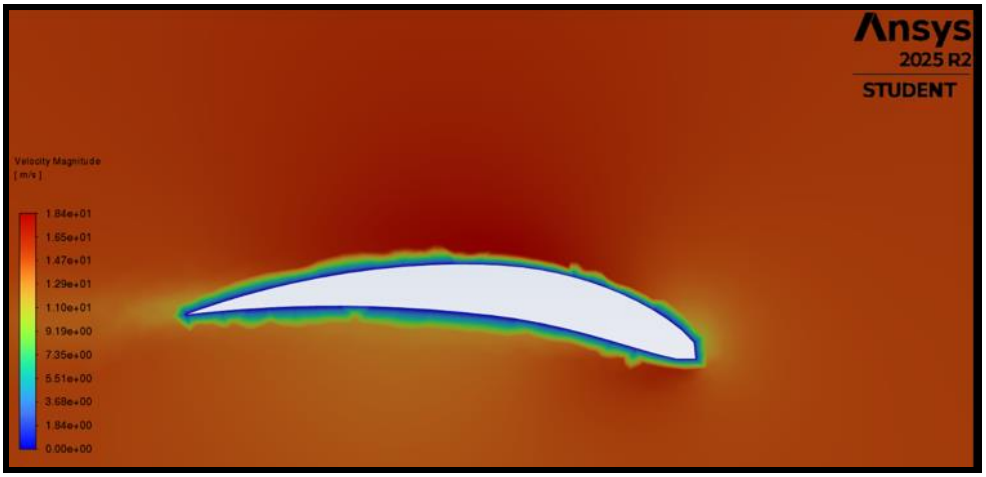

Fig 27: Symmetrical Hummingbird Velocity Magnitude at 15 *m/s*

The static pressure distribution (Fig. 28) for the symmetrical hummingbird wing at 15 *m/s* highlights a clear pressure differential between the upper and lower surfaces of the wing. The contours reveal lower static pressure over the upper surface, particularly concentrated around the leading edge and mid-chord region, while the underside retains relatively higher values of pressure. This pressure gradient is the primary driver of lift, as it generates an upward force that balances the increased aerodynamic load at higher velocities. At 15 *m/s*, the pressure contours also indicate stronger suction peaks near the leading edge, which stabilise into smoother gradients along the chord length. This behaviour is consistent with the ability of symmetrical wing sections to manage flow symmetrically without inducing excessive asymmetry or stall at moderate angles of attack. For bio-inspired applications, this mirrors how hummingbird wings exploit pressure differences to sustain efficient lift during both hovering and forward flapping, adapting effectively across a wide flight envelope.

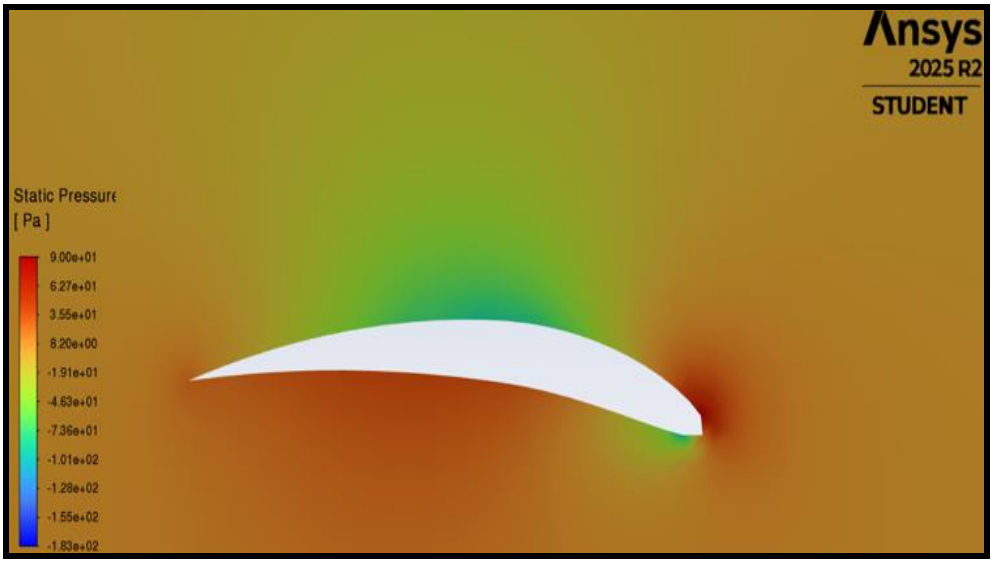

Fig 28: Symmetrical Hummingbird Static Pressure at 15 *m/s*

5.4. Comparison of all 3 Cases (Inlet free stream air velocities of 5 m/s, 10 m/s, 15 m/s)

The results across the three inlet velocities provide a clear indication of how the aerodynamic behaviour of the hummingbird-inspired wing develops with increasing flow speed. At the lowest velocity of 5 *m/s*, the lift and drag forces were relatively small, as expected from the reduced dynamic pressure. The flow remained relatively stable, with smooth contour gradients evident in both velocity and pressure fields. At this velocity, the wing demonstrated its ability to sustain a modest lift force, which is crucial for low-speed manoeuvrability and hovering-type conditions. This mirrors the biological role of hummingbirds, where low flight speeds require steady but efficient force generation to maintain stability without inducing significant drag. When the inlet velocity was increased to 10 *m/s*, a notable enhancement in lift generation was observed. The lift iteration graph demonstrated a sharper rise and

faster stabilisation compared to 5 *m/s*, reflecting the direct proportionality between velocity and lift under incompressible flow conditions. Pressure contours revealed a more pronounced suction effect on the upper surface, while velocity contours highlighted accelerated flow regions above the leading edge. This combination suggests that the wing begins to exploit its geometry more effectively at intermediate speeds. For bio-inspired UAV applications, this velocity range demonstrates where the wing design transitions from low-speed hovering performance to efficient forward flight, offering both stability and enhanced aerodynamic efficiency. The drag results at this speed showed that although drag increased, its growth rate was less significant compared to lift, resulting in a more favourable lift-to-drag ratio. At 15 *m/s*, the aerodynamic forces reached their highest magnitudes, with lift significantly exceeding the values obtained at lower velocities. The lift coefficient, however, exhibited a more stabilised behaviour, indicating that while absolute forces increased due to dynamic pressure, the aerodynamic efficiency of the wing did not scale linearly, as noted in Song *et al*. [19] and Dong *et al.* [21]. These studies however did not visualize the 3-D aerodynamic flow on gliding hummingbird inspired UAV wings. However, they did show lift and drag behaviour which concurs with our findings. The general trends in these studies also agree with the computed patterns we have produced in the ANSYS FLUENT simulations, although full flapping is not considered in our study. This reflects a fundamental aerodynamic principle: higher speeds enhance force generation, but they also impose penalties in terms of drag and flow complexity. The drag iteration results showed greater initial spikes before stabilisation, suggesting that the wing was subjected to stronger resistive forces, particularly due to increased flow interaction with the surface. Pressure contours illustrated intensified suction peaks near the leading edge, while velocity fields highlighted more energetic flow over the upper surface. Importantly, the symmetrical wing analysis at this speed revealed how bio-inspired geometries balance the aerodynamic load without excessive asymmetry, making them well-suited for sustained forward flight in UAV contexts. When the three velocities are compared, the results demonstrate a clear scaling effect consistent with aerodynamic theory. At 5 *m/s*, the wing operates in a low-energy regime, suitable for hovering or energy-efficient loitering. At 10 *m/s*, performance transitions to a more balanced state, where lift generation is efficient relative to drag, aligning with practical forward-flight scenarios for UAVs. At 15 *m/s*, the design reaches its upper operating regime within the tested range, producing strong aerodynamic forces that could support greater payloads or higher-speed manoeuvres but at the cost of increased drag and more complex flow behaviour.

5.5. Comparison to Literature

These findings highlight the versatility of the hummingbird-inspired design. In nature, hummingbirds adapt their wing kinematics to exploit aerodynamic benefits across a wide speed range, from hovering at low velocities to darting movements at higher speeds. Similarly, the CFD analysis suggests that such a bio-inspired wing could provide UAVs with comparable adaptability, allowing operation in diverse flight conditions without requiring entirely different wing configurations. The results therefore support the hypothesis that nature-inspired designs can bridge the gap between stability at low speeds and efficiency at higher speeds, a feature that is highly desirable in micro-air vehicle development. The velocity and pressure contours obtained in this study showed clear regions of accelerated flow above the wing surface, coupled with low-pressure zones that contributed significantly to lift generation. This behaviour is consistent with experimental observations of hovering hummingbirds, where Warrick *et al.* [24] reported that approximately 75% of the weight support was generated during the downstroke by the attachment of a stable leading-edge vortex (LEV). Flow separation occurs when the boundary layer detaches from the wing surface due to adverse pressure gradients, although this has not been computed in our case, and relatively stable flow patterns were observed. In fixed-wing configurations, the flow separation phenomenon is mostly observed near the trailing edge during high angle of attack operations. The onset of separation reduces lift and increases drag, potentially triggering stall conditions. The current study is confined to low angles of attack, however. The contours presented in this current study, while confined to gliding flight and not flapping flight of microUAVs, however, do capture key aerodynamic characteristics which are relevant to bio-inspired lift production. Further comparison can be made with the work of Dong *et al.* [20] who demonstrated through dynamic morphing simulations that the LEV remained attached during the downstroke but was shed more rapidly in the upstroke, creating asymmetry in force production. This directly supports the CFD observations in this study, where pressure fields around the wing showed stronger suction peaks during forward motion, highlighting how flow attachment and detachment cycles regulate lift and drag across flapping phases. The influence of asymmetry in vortex strength has also been reported by Menzer *et al.* [25], who reconstructed hummingbird wing kinematics and found that asymmetric motion produced up to 59% variation in LEV strength between inner and outer wing regions. Such findings provide an external benchmark to explain the non-uniform contour distributions observed in the present results, particularly the differences in suction intensity across the span of the wing.

6. Conclusions and Future pathways

In this article, ANSYS FLUENT computational fluid dynamics simulations have been conducted to study the aerodynamics of a hummingbird-inspired wing for micro-UAV applications. The study has focused on the wing aerodynamic efficiency across varying flow conditions i.e. inlet free stream velocities (5 *m/s*, 10 *m/s*, and 15 *m/s*). By combining the outcomes of computational simulations with theoretical aerodynamic principles, the study provides deeper insights into the aerodynamic performance of bio-inspired wings and their potential role in micro-unmanned aerial vehicle (MAV) design. Furthermore, the study highlights the broader implications of these findings, outlining both the strengths of the hummingbird-inspired model and the limitations that warrant future investigation.

6.1. Summary of key findings and insights

The results demonstrated that the hummingbird-inspired wing generates consistent lift and stable flow patterns across all tested velocities, though the magnitude of lift and drag was shown to vary depending on inlet speed. At 5 *m/s*, the wing achieved a modest lift output with minimal drag, indicating efficient aerodynamic behaviour under low-speed conditions. At 10 *m/s*, lift production increased significantly, with the flow visualisations showing stronger velocity gradients and pressure differentials across the wing surfaces. At 15 *m/s*, lift was maximised, though this was accompanied by an increase in drag, reflecting the classical aerodynamic trade-off between force generation and resistance. The comparative analysis of symmetrical and full 3-D wing models revealed that symmetry-based half-wing simulations effectively captured the aerodynamic behaviour while reducing computational cost. The pressure contours showed the expected regions of high pressure below the wing and low pressure above it, which became more pronounced with increasing velocity. This behaviour closely resembles the aerodynamic mechanisms used by natural hummingbirds, where the balance between strong pressure gradients and efficient velocity distribution allows for sustained hovering and forward flight. The contour plots also highlighted the importance of velocity magnitude and pressure distributions in shaping the aerodynamic forces experienced by the bio-inspired wing. Strong velocity acceleration over the upper wing surface, particularly at higher speeds, confirmed the presence of enhanced suction effects, which are critical to lift generation. Conversely, higher static pressure concentrations near the leading edge and trailing regions at elevated velocities were found to contribute to increased drag. This interplay between lift enhancement and drag penalties reflects the biological optimisation of hummingbird wings, which prioritise lift generation to sustain hovering but at the cost of higher energy expenditure. These findings emphasise the effectiveness of the hummingbird-inspired design in replicating natural flight mechanics. The wing was shown to be capable of carrying higher aerodynamic loads compared to smaller insects such as the housefly, due to its larger span and aspect ratio. However, this advantage comes with the requirement of greater power input, a factor also observed in natural hummingbird flight, where rapid wingbeats demand high metabolic energy. The study therefore reinforces the bio-inspired principle that wing morphology is a compromise between aerodynamic efficiency and energetic cost.

6.2. Future pathways

A key area for improvement lies in establishing a direct comparison with a conventional fixed-wing geometry. By simulating a standard rigid aerofoil, such as a thin cambered plate or a low-Reynolds-number aerofoil commonly used in micro-air vehicles, a baseline could be obtained for benchmarking. This would allow the aerodynamic benefits and trade-offs of the hummingbird-inspired wing to be explicitly quantified against a more traditional design. For instance, a fixed wing would likely demonstrate superior efficiency at higher forward speeds due to reduced drag, whereas the hummingbird-inspired geometry may retain advantages at low Reynolds numbers where unsteady or separated flow dominates. Such a comparison would not only strengthen the conclusions but would also contextualise the biological relevance of the hummingbird wing within the engineering domain of UAV design. Future work should also move beyond steady-state simulations and consider time-accurate unsteady analyses to capture flapping kinematics more faithfully. Hummingbirds exploit unsteady mechanisms such as rotational circulation, wake capture, and leading-edge vortex (LEV) stabilisation, which cannot be fully observed in static simulations. Incorporating prescribed flapping motions through dynamic meshing or overset grids would provide a more realistic representation of their natural flight and allow the role of these unsteady effects in lift generation to be quantified. Another key area for improvement lies in the complexity of the wing model itself. The present study employed a rigid geometry; however, real hummingbird wings exhibit flexibility and structural compliance, enabling passive shape adaptation to the surrounding flow. Future simulations could incorporate fluid–structure interaction (FSI) models to investigate how wing flexibility influences aerodynamic efficiency, stability, and energy expenditure. This would align the computational model more closely with biological reality and could reveal passive mechanisms that may be transferable to bio-inspired UAVs. From a methodological standpoint, improvements could

also be made through enhanced turbulence modelling and transitional flow prediction. At the low Reynolds numbers considered in this study, laminar–turbulent transition plays a crucial role in determining boundary layer behaviour. Future work may explore employ transition-sensitive turbulence models in ANSYS FLUENT, to better capture separation bubbles and subtle flow structures that strongly influence lift and drag at this scale.

Acknowledgements
The authors are grateful to the reviewer for his/her comments which have added clarity to the present work.

References

[1] D. W. Bechert, M. Bruse, W. Hage, R. Meyer, Fluid mechanics of biological surfaces and their technological application, *naturwissenschaften,* Vol. 87, No. 4, pp. 157-171, 2000, 2000.
[2] R. E. Brown, M. R. Fedde, Airflow sensors in the avian wing, *Journal of Experimental Biology,* Vol. 179, No. 1, pp. 13-30, 1993, 1993.
[3] W. Shyy, Y. Lian, J. Tang, H. Liu, P. Trizila, B. Stanford, L. Bernal, C. Cesnik, P. Friedmann, P. Ifju, Computational aerodynamics of low Reynolds number plunging, pitching and flexible wings for MAV applications, *Acta Mechanica Sinica,* Vol. 24, No. 4, pp. 351-373, 2008, 2008.
[4] H. Chen, F. Rao, X. Shang, D. Zhang, I. Hagiwara, Biomimetic drag reduction study on herringbone riblets of bird feather, *Journal of Bionic Engineering,* Vol. 10, No. 3, pp. 341-349, 2013, 2013.
[5] H. Chen, F. Rao, X. Shang, D. Zhang, I. Hagiwara, Flow over bio-inspired 3D herringbone wall riblets, *Experiments in Fluids,* Vol. 55, No. 3, 2014, 2014.
[6] K. Chen, Q. Liu, G. Liao, Y. Yang, L. Ren, H. Yang, X. Chen, The sound suppression characteristics of wing feather of owl (bubo bubo), *Journal of Bionic Engineering,* Vol. 9, No. 2, pp. 192-199, 2012, 2012.
[7] S. Klän, T. Bachmann, M. Klaas, H. Wagner, W. Schröder, Experimental analysis of the flow field over a novel owl based airfoil, *Experiments in Fluids,* Vol. 46, No. 5, pp. 975-989, 2009, 2009.
[8] H. Eder, W. Fiedler, M. Neuhäuser, Evaluation of aerodynamic parameters from infrared laser tracking of free-gliding white storks, *Journal of Ornithology,* Vol. 156, No. 3, pp. 667-677, 2015, 2015.
[9] K. E. Crandell, B. W. Tobalske, Aerodynamics of tip-reversal upstroke in a revolving pigeon wing, *Journal of Experimental Biology,* Vol. 214, No. Pt 11, pp. 1867-1873, 2011, 2011.
[10] A. Ennos, J. Hickson, A. Roberts, Functional morphology of the vanes of the flight feathers of the pigeon Columba livia, *Journal of Experimental Biology,* Vol. 198, No. Pt 5, pp. 1219-1228, 1995, 1995.
[11] C. Ge, L. Ren, P. Liang, C. Zhang, Z. Zhang, High-lift effect of bionic slat based on owl wing, *Journal of Bionic Engineering,* Vol. 10, No. 4, pp. 456-463, 2013, 2013.
[12] S. Ito, Aerodynamic influence of leading-edge serrations on an airfoil in a low Reynolds number - A study of an owl wing with leading edge serrations -: - A study of an owl wing with leading edge serrations, *Journal of Biomechanical Science and Engineering,* Vol. 4, No. 1, pp. 117-123, 2009, 2009.
[13] P. C. Withers, An aerodynamic analysis of bird wings as fixed aerofoils, *Journal of Experimental Biology,* Vol. 90, No. 1, pp. 143-162, 1981, 1981.
[14] D. L. Altshuler, R. Dudley, Kinematics of hovering hummingbird flight along simulated and natural elevational gradients, *Journal of Experimental Biology,* Vol. 206, No. Pt 18, pp. 3139-3147, 2003, 2003.
[15] T. Nakata, H. Liu, Y. Tanaka, N. Nishihashi, X. Wang, A. Sato, Aerodynamics of a bio-inspired flexible flapping-wing micro air vehicle, *Bioinspiration & Biomimetics,* Vol. 6, No. 4, pp. 045002, 2011, 2011.
[16] C. P. Ellington, The novel aerodynamics of insect flight: applications to micro-air vehicles, *Journal of Experimental Biology,* Vol. 202, No. Pt 23, pp. 3439-3448, 1999, 1999.
[17] H. Zhu, and Yang Zhang., Effect of morphological characteristics on the aerodynamic performance of a flexible flapping butterfly wing, *Physics of Fluids,* Vol. 37, 2025, 2025.
[18] A. T. Song, X., Hedrick, T.L., Wing-wake interaction of a hovering hummingbird, *Proceedings of the Royal Society B: Biological Sciences,* Vol. 281, 1788, 1788.
[19] L. Liu, M. Sun, The added mass forces in insect flapping wings, *Journal of Theoretical Biology,* Vol. 437, pp. 45-50, 2018, 2018.
[20] Y. Dong, B. Song, D. Xue, Y. Li, W. Yang, Numerical study of the aerodynamics of a hovering hummingbird's wing with dynamic morphing, *International Journal of Aerospace Engineering,* Vol. 2022, pp. 1-17, 2022, 2022.
[21] J. E. Matsson, 2022, *An introduction to ANSYS fluent 2022*, SDC Publications, Mission, KS
[22] J. L. Palmer, M. B. Jones, J. Drobik, Design elements of a bio-inspired micro air vehicle, *IFAC Proceedings Volumes,* Vol. 46, No. 10, pp. 235-241, 2013, 2013.

[23] H. V. Phan, H. C. Park, Insect-inspired, tailless, hover-capable flapping-wing robots: Recent progress, challenges, and future directions, *Progress in Aerospace Sciences,* Vol. 111, No. 100573, pp. 100573, 2019, 2019.

[24] D. R. Warrick, B. W. Tobalske, D. R. Powers, Aerodynamics of the hovering hummingbird, *Nature,* Vol. 435, No. 7045, pp. 1094-1097, 2005, 2005.

[25] A. Menzer, Y. Ren, J. Guo, B. W. Tobalske, H. Dong, Wing kinematics and unsteady aerodynamics of a hummingbird pure yawing maneuver, *Biomimetics (Basel),* Vol. 7, No. 3, pp. 115, 2022, 2022.